JOURNAL OF GEOPHYSICAL RESEARCH, VOL. 99, NO. B10, PAGES 19,719–19,740, OCTOBER 10, 1994

Magmatic processes at a slow spreading ridge segment: 26°S Mid-Atlantic Ridge

Yaoling Niu[1]

Lamont-Doherty Earth Observatory, Palisades, New York

Rodey Batiza

Department of Geology and Geophysics, University of Hawaii at Manoa, Honolulu

Abstract. We present new data on the mineralogy, and major and trace element compositions of lavas dredged along a segment of the Mid-Atlantic Ridge at ~26°S. This segment is bounded on the north by the Rio Grande transform and on the south by the Moore discontinuity and has an along-axis, central high rising to ~2600 m near the middle of the segment. The segment is well-studied and the dredges are spaced ~7 km apart. The lavas are exclusively normal mid-ocean ridge basalt (N-MORB), with a limited range of MgO (8.62–6.55 wt %). Petrographically, the lavas are dominated by low-pressure mineral assemblages, with two distinct crystallization sequences: Type I basalts have pl → pl + ol → pl + ol + cpx and come mainly from the interior of the segment; type II basalts, mainly from near the offsets, have ol → ol + pl → ol + pl + cpx. Some of the lavas contain rare anorthitic megacrysts and one sample contains a small gabbroic inclusion. The mineralogy and mineral chemistry are typical of N-MORB lavas elsewhere. Type I lavas have higher CaO and lower FeO, TiO_2, and Na_2O than type II, but similar Al_2O_3 contents. Type I lavas define curvilinear trends on MgO variation diagrams and represent diverse parental melts that have undergone variable extents of low-pressure fractionation. In contrast, type II lavas exhibit less fractionation and more diversity of inferred parental melt compositions. Fractionation of all the lavas appears to have been mainly at low pressure, though we cannot rule out the possibility of some higher-pressure, polybaric crystallization. Except for lavas near the offsets, there is a rough correlation of lava chemistry and axial depth, defining along-axis "W" and "M" patterns. We infer that the center of the segment has higher magma supply than the ends and that magma chambers in the center are larger and more like those at the East Pacific Rise than those near offsets. Overall, the segment is fed by diverse magma types with different melting histories that retain their chemical distinctiveness all the way to the surface. Ni, $[La/Sm]_N$, and other trace elements also display "W" patterns, as do isotope ratios, but the patterns are noisier than those of the major elements. We infer that the mantle source of the lavas is heterogenous but its range of variability in major and trace elements and isotope ratios appears to be small. The rare earth elements and major elements normalized to 8 wt % MgO exhibit U-shaped along-axis variation patterns. Calculations show that the along-axis initial depth of melting is constant at ~50 km but that the final depth of melting varies from ~35 km near offsets to ~28 km in the center. The mean extent of melting varies from 15% near offsets to 18% in the center and correlates with values of the mantle Bouguer anomaly, suggesting that the gravity pattern is of shallow feature (< 50 km). We suggest that the melting patterns and density structure result from the combined effect of along-axis variation in mantle upwelling and melt production and the cold edges near offsets. The 26°S segment exhibits the local trend of chemical variation. New chemical evidence (Ca, Ti, and Ni data) strengthens the hypothesis that the local trend at slow spreading ridges is due to the melting reaction: melt A + pyroxene ⇒ melt B + olivine. We suggest that this reaction, occurring in ascending and melting diapirs, is an important process at slow spreading ridges, consistent with gravity and modeling studies.

Introduction

The oceanic crust is produced by mid-ocean ridges at a wide range of rates and represents the net product of both magmatic and tectonic processes operating within and below the plate boundary zone. For many years, the observed differences in morphology [e.g., *Macdonald*, 1982] and basalt chemistry [e.g., *Nisbet and Pearce*, 1973; *Morel and Hékinian*, 1980; *Natland*, 1980; *Flower*, 1980] between fast and slow spreading ridges hinted at fundamental differences in these processes resulting from differences in spreading rate. Recent gravity [*Lin et al.*, 1990; *Lin and Phipps Morgan*, 1992] and modeling studies [*Parmentier and Phipps Morgan*, 1990; *Turcotte and Phipps Morgan*, 1992; *Scott*, 1992, and references therein] provide additional strong support for this notion and indicate that differences in spreading rate may control the fundamental style of mantle upwelling beneath the ridge. Since melting

[1]Also at Department of Earth Sciences, University of Queensland, Brisbane, Queensland, Australia.

Paper number 94JB01663.
0148-0227/94/94JB-01663$05.00

results from the passive and/or buoyant upwelling of mantle material, it is to be expected that differences in mantle upwelling might lead to differences in melting, melt migration and segregation, and magma storage [e.g., *Sinton and Detrick*, 1992] below fast and slow-spreading ridges. Indeed, *Niu and Batiza* [1993] show that the chemical systematics of fast and slow ridges differ markedly and argue that this difference is due to a basic difference in the geometry of mantle upwelling: being more two-dimensional (2-D) below fast ridges and more three-dimensional (3-D) below slow ones.

In this paper, we present new major and trace element data for a slow spreading ridge segment of the southern Mid-Atlantic Ridge near 26°S. This study is a companion to the study of *Batiza and Niu* [1992] for the fast spreading East Pacific Rise near 9°30'N. The new data we present provide additional constraints and insight into the nature of magmatic processes occurring beneath slow spreading ridges.

Previous Work in the 26°S Area

The ridge axis of the Mid-Atlantic Ridge near 26°S and its flanks out to 5–7 Ma have been well studied using Sea Beam [*Grindlay et al.*, 1991, 1992], magnetics [*Carbotte et al.*, 1991; *Grindlay et al.*, 1992] and gravity [*Blackman and Forsyth*, 1991]. The ridge segment at ~26°S is about 100 km long and is bounded by the Rio Grande transform (north) and the Moore discontinuity (south). It spreads slightly asymmetrically at rates of ~19.3 mm/yr to the west and ~16.3 mm/yr to the east [*Carbotte et al.*, 1991]. Like the Mid-Atlantic Ridge segments between 27°N and 32°N [*Lin et al.*, 1990; *Sempéré et al.*, 1990] and 31°S–34°S MAR [*Carbotte et al.*, 1991; *Grindlay et al.*, 1991; *Michael et al.*, 1994], the 26°S segment is characterized by an along-axis topographic high which rises to ~2600 m near the center of the segment. To the north and south of this high, the axis deepens rapidly to ~4100 m near the offsets. At both ends, the segment has a well-developed axial rift valley up to 25 km wide and 1.5 km deep that shallows and eventually vanishes at the latitude of the along-axis high. Interestingly, the present central topographic high appears to be related to discrete, off-axis bathymetric highs forming a north pointing V-shaped pattern, suggesting its northward migration in the past several million years (see *Blackman and Forsyth* [1991] and *Grindlay et al.* [1992] for details).

The fine scale morphology of the rift valley floor is described in detail by *Grindlay et al.* [1992] and is quite variable. The magnetically defined axis occurs variably along linear topographic highs, linear topographic lows and small seamounts of the type described by *Smith and Cann* [1990]. The tectonic history of the segment has been fairly complex, especially at the southern end where the character and offset distance of the Moore discontinuity has varied greatly in the past [*Carbotte et al.*, 1991; *Grindlay et al.*, 1991, 1992]. Another complication is the presence of a small, probably inactive discontinuity, called the Midway discontinuity, at 26°12'S [*Grindlay et al.*, 1992]. While this feature has little topographic expression in the present rift valley floor and no petrologic expression, it does show up as a feature in the magnetization maps and may have been important in the past [*Grindlay et al.*, 1992].

Previous regional studies of the southern Mid-Atlantic Ridge (MAR) [*Humphris et al.*, 1985; *Schilling et al.*, 1985; *Hanan et al.*, 1986] indicate that the ridge at 26°S is unaffected by mantle plume activity and is thus a "normal" ridge segment. Preliminary petrologic data from the 26°S axis segment and nearby seamounts were reported by *Batiza et al.* [1988, 1989, 1990] and *Castillo and Batiza* [1989]. These preliminary studies showed the presence of regular along-axis variations in chemistry (with relatively simple "W" and "M" shapes) as well as chemical systematics that have come to be known as the local trend [*Klein and Langmuir*, 1989]. The new data we present here extend these preliminary findings and allow additional interpretations.

Results and Interpretations

Dredges

Figure 1 shows the dredge locations, with an average spacing of ~7 km. Table 1 details the dredge information, including whether the dredge is located on or off axis, as defined magnetically by *Grindlay et al.* [1992]. While the location of the neovolcanic axis is not known precisely (e.g., from detailed bottom studies) the magnetic axis probably gives the best estimate of its location. All the dredges were navigated using Sea Beam and are within 1–2 km of the magnetic axis. The amount of rock recovered in each dredge is quite variable but all the dredges recovered very fresh glass, with little (< 2 mm) or no manganese coating. Most of the dredged samples are fragments of pillow lavas, although rare sheet flows also occur. Two samples from dredge 12 (D12–2, 3) are hyaloclastites, consisting of 1 – 4 mm glass shards cemented in altered, greenish, clay-rich matrix.

Petrography

In thin section, the samples vary from aphyric to sparsely phyric to moderately phyric, without geographic order. Phenocryst assemblages are variable, including olivine only, olivine + plagioclase, and olivine + plagioclase + clinopyroxene, with or without spinel. Groundmass materials include glass, glassy spherulites, glassy mesostasis, and microlitic plagiocalse, olivine, clinopyroxene. On the basis of textural relationships, we find two distinct crystallization sequences among the samples. Some rocks (type I) crystallize plagioclase first, followed by olivine and then clinopyroxene; these are confined to dredges 14-19, 21, and 22, mostly from the interior of the segment (Figure 1). Other rocks (type II) have olivine first, followed by plagioclase and then clinopyroxene; these occur in dredges 12, 13, 20, and 23–27, mostly but not exclusively from near the offsets (Figure 1). Later, we show that these two groups also correspond to chemical groupings, which probably accounts for the difference in the order of appearance of olivine and plagioclase.

Olivine phenocrysts vary in size from 200 μm to 800 μm, and are euhedral, subhedral, anhedral, and skeletal. They show a limited compositional range (Fo_{88} to Fo_{82}) and most crystals are relatively homogeneous. Olivines within single samples have limited compositional variation as shown in Figure 2 (also see Table 2), suggesting that they are in equilibrium with the host melt. In one sample (D12-29), however, two types of olivine crystals are observed, one euhedral, the other with embayed form characteristic of resorption. The latter show slight reverse zoning (Fo ~ 82 in the core and Fo ~ 85 at the rim) that may indicate mixing or assimilation.

Plagioclase phenocrysts vary in length from <200 μm to ~ 1 mm and are euhedral, subhedral, and skeletal. The composition

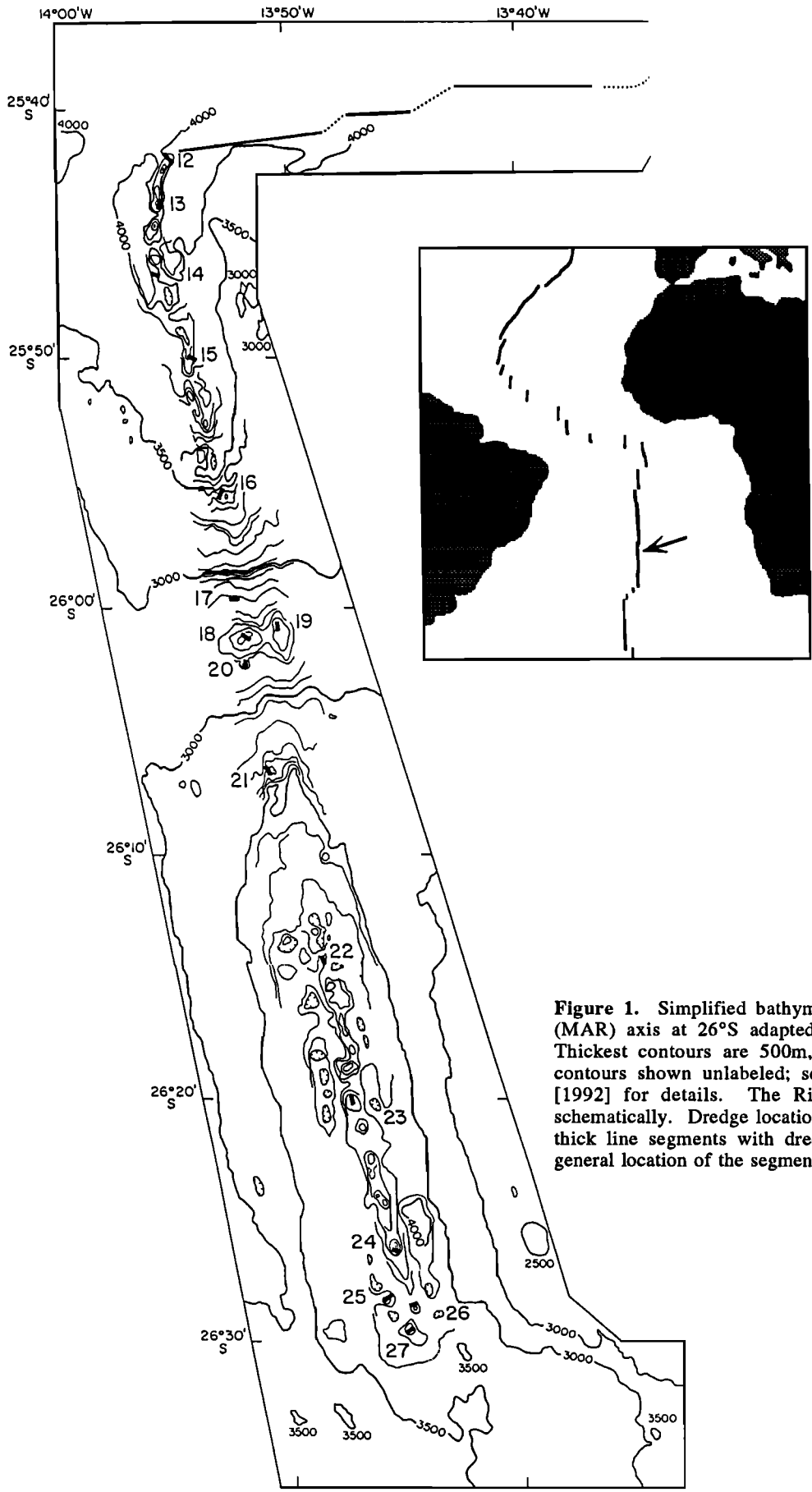

Figure 1. Simplified bathymetry of the Mid-Atlantic Ridge (MAR) axis at 26°S adapted from *Grindlay et al.* [1992]. Thickest contours are 500m, with selected 100m and 25m contours shown unlabeled; see Figure 2 of *Grindlay et al.* [1992] for details. The Rio Grande transform is shown schematically. Dredge locations (Table 1) are shown as short, thick line segments with dredge numbers. Inset shows the general location of the segment at the Mid-Atlantic Ridge.

Table 1. Dredge Information

Dredge	Start		End		Distance,	Location*	Depth,	Amount of
	Latitude	Longitude	Latitude	Longitude	m		m	Rock, kg
D12	25°42.00'S	13°54.65'W	25°41.90'S	13°54.83'W	353	cone on axis	4000-3960	90
D13	25°43.87'S	13°55.35'W	25°43.75'S	13°55.35'W	222	cone on axis	3940-3900	50
D14	25°46.50'S	13°55.10'W	25°46.30'S	13°55.40'W	623	on axis	4010-3960	3
D15	25°49.95'S	13°54.12'W	25°50.20'S	13°54.22'W	492	cone 1 km east of axis	3960-3880	4
D16	25°55.70'S	13°53.20'W	25°55.40'S	13°53.00'W	648	on axis	3470-3460	10
D17	25°59.75'S	13°52.60'W	25°59.75'S	13°52.30'W	499	1.5 km west of axis	2680-2670	13
D18	26°01.20'S	13°52.08'W	26°01.35'S	13°52.30'W	460	cone 1.5 km west of axis	2510	22
D19	26°00.85'S	13°50.62'W	26°00.60'S	13°50.62'W	463	cone 1.0 km east of axis	2520	15
D20	26°02.16'S	13°52.13'W	26°02.40'S	13°52.03'W	475	cone 2.0 km west of axis	2580-2830	0.2
D21	26°07.09'S	13°51.70'W	26°06.80'S	13°51.80'W	562	cone 2.0 km west of axis	3390-3370	10
D22	26°13.85'S	13°48.55'W	26°13.48'S	13°48.77'W	777	cone 1.7 km east of axis	3800-3770	20
D23	26°19.94'S	13°47.64'W	26°19.68'S	13°47.70'W	492	cone 2.0 east of axis	3700-3710	2
D24	26°26.15'S	13°45.80'W	26°26.22'S	13°45.65'W	281	cone 1.8 km east of axis	3480	10
D25	26°28.25'S	13°46.30'W	26°28.20'S	13°46.02'W	473	cone on axis	3770-3750	1
D26	26°28.32'S	13°45.08'W	26°28.38'S	13°44.80'W	477	cone 2.2 km east of axis	3770-3780	0.2
D27	26°29.60'S	13°45.30'W	26°29.60'S	13°45.30'W	<10	cone 1.6 east of axis	3700	1

*Axial location taken from *Grindlay et al.* [1992]. See text for discussions.

of plagioclase phenocrysts (Figure 3 and Table 3) varies greatly within single samples. As expected, chemical zonation is a common feature, but Figure 3 and Table 3 show that zoning can either be normal or reverse. More commonly the zoning patterns are highly variable, a ubiquitous petrographic feature of MORB [e.g., *Bryan et al.*, 1981; *Bryan*, 1983; *Davis and Clague*, 1987; *Batiza and Niu*, 1992].

Some samples (15-4, 16-2, 17-5, 18-5, and 20-4) contain individual plagioclase grains and/or aggregates that do not appear to be normal phenocrysts. These are characterized by large size (up to 3 mm), rounded or irregular outlines, variably developed sieve texture, and high An contents (up to An_{93}, see Figure 3 and Table 3). These crystals are similar to those previously described by *Rhodes et al.* [1979] and *Bryan et al.* [1981] from other segments of the Mid-Atlantic Ridge and by *Davis and Clague* [1987] from the Gorda ridge. Such crystals are obviously not in equilibrium with their present host melts and have previously been interpreted to be either the product of early crystallization from more primitive magmas [*Fisk et al.*, 1982] or crystallization at higher pressure [*Bender et al.*, 1984]. We tend to favor the interpretation of *Fisk et al.* [1982] because high-pressure crystallization produces Ab-rich, not An-rich plagioclase [*Fram and Longhi*, 1992]. On the other hand, it is possible that initially albitic, high-pressure plagioclase could become An-rich as a result of decompression during melt transport to produce the observed megacrysts (R. Neilsen, personal communication, 1993).

Phenocrysts of clinopyroxenes are rare in the 26°S lavas, but quench crystals are very common away from glassy margins and in pillow interiors, especially in samples with MgO < 7.5 wt %. These observations suggest that the melts became saturated with clinopyroxene at low pressure. The quench crystals have variable prismatic forms, ~100 μm to ~600 μm long and usually less than 20 μm wide. Table 4 shows that

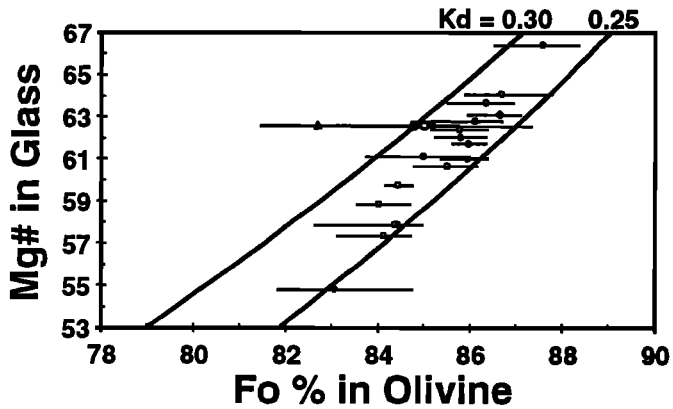

Figure 2. Olivine analyses plotted against the Mg/(Mg + Fe^{2+}) of host glass ($Fe^{2+}/[Fe^{2+}+Fe^{3+}]$ = 0.9 is assumed). For reference, we show the calculated Kd ($Fe\text{-}Mg^{ol\text{-}liq}$) values of 0.25 and 0.30. The open circles are mean compositions, and the line segments represent the observed variation range in the individual samples. The large open circle is the mean composition of the euhedral type in D12-29. The solid square, solid triangle, and the lines represent the mean compositions and the ranges of the rims and cores of anhedral type in D12-29. The solid diamond and the line represent the mean composition and the range of the crystal clot in D18-4. Note that most olivines are in equilibrium with their host melt with a mean K_d value ~0.27 [*Roeder and Emslie*, 1970] (see text for discussion).

Table 2. Representative Probe Microanalyses of Olivine

	D12-29			D14-1	D15-2	D15-4	D16-2	D17-5	D18-4	D18-5	D20-4	D21-4	D21-5	D21-6	D22-2	D23-6	D24-1	D25-1	D27-1
	Euhedral	Rim	Core						(clot)										
N	8	12	11	29	17	22	23	23	13	17	6	16	10	14	11	10	14	17	20
SiO_2	39.20	39.79	39.32	39.89	40.00	39.88	40.00	40.06	40.19	40.01	40.43	40.30	40.22	39.88	39.39	39.53	39.82	39.83	39.86
FeO	13.52	13.75	15.78	14.94	14.62	14.84	13.59	13.01	12.40	13.54	12.54	11.30	12.98	13.76	15.25	14.33	13.00	12.74	12.51
MnO	0.24	0.22	0.29	0.29	0.30	0.32	0.27	0.23	0.24	0.23	0.20	0.19	0.25	0.25	0.28	0.26	0.22	0.23	0.23
MgO	45.31	45.56	43.99	45.15	45.48	45.19	45.95	46.43	47.51	46.49	47.60	48.02	46.71	46.26	44.97	45.61	46.35	46.52	46.68
CaO	0.38	0.46	0.29	0.08	0.03	0.04	0.04	0.25	0.34	0.30	0.29	0.32	0.41	0.34	0.35	0.33	0.34	0.30	0.35
Total	98.65	99.78	99.67	100.36	100.43	100.27	99.85	99.98	99.88	100.57	101.07	100.14	100.57	100.49	100.24	100.06	99.74	99.62	99.63
Si	0.994	0.997	0.996	0.998	0.998	0.998	1.000	0.998	0.992	0.993	0.994	0.995	0.996	0.992	0.990	0.991	0.995	0.995	0.995
Fe^{2+}	0.286	0.288	0.334	0.312	0.305	0.310	0.284	0.270	0.256	0.281	0.257	0.233	0.268	0.286	0.320	0.300	0.271	0.266	0.261
Mn	0.005	0.005	0.006	0.006	0.006	0.007	0.006	0.005	0.005	0.005	0.004	0.004	0.005	0.005	0.006	0.006	0.005	0.005	0.005
Mg	1.711	1.701	1.660	1.683	1.691	1.685	1.710	1.723	1.747	1.720	1.743	1.765	1.723	1.715	1.684	1.704	1.725	1.731	1.735
Ca	0.010	0.012	0.008	0.002	0.001	0.001	0.001	0.007	0.009	0.008	0.008	0.009	0.011	0.009	0.010	0.009	0.009	0.008	0.009
ΣCations	3.006	3.003	3.004	3.002	3.002	3.002	3.000	3.002	3.008	3.007	3.006	3.005	3.004	3.008	3.010	3.009	3.005	3.005	3.005
Fo	0.850	0.848	0.827	0.840	0.844	0.841	0.855	0.859	0.866	0.854	0.866	0.878	0.858	0.851	0.834	0.844	0.858	0.861	0.863
Fa	0.142	0.143	0.166	0.156	0.152	0.155	0.142	0.135	0.127	0.139	0.128	0.116	0.134	0.142	0.158	0.149	0.135	0.132	0.130
Ca-Ol	0.005	0.006	0.004	0.001	0.000	0.000	0.001	0.003	0.004	0.004	0.004	0.004	0.005	0.005	0.005	0.004	0.004	0.004	0.005
Mn-Ol	0.003	0.002	0.003	0.003	0.003	0.003	0.003	0.002	0.003	0.002	0.002	0.002	0.003	0.003	0.003	0.003	0.002	0.002	0.002

N is number of analyses averaged. Analyses were done at the University of Hawaii, Honolulu. Note rim and core for D12-29 refer to one type of olivine which exhibits resorption features characterized by reverse zoning (see text for discussion).

there exist small but significant compositional variations among grains in a single thin section. However, as shown in Figure 4, variations in Wo component are much more important than Fe-Mg variations, a characteristic feature of quench crystals [e.g., *Grove and Bryan*, 1983; *Stakes et al.*, 1984] due to rapid cooling [*Mevel and Velde*, 1976; *Grove and Bryan*, 1983]. Very fine grained spinel (< 50 μm) may be found either in the groundmass or as inclusions in olivine in primitive type II samples.

One additional interesting petrographic feature of the lavas is a crystalline clot found in type I sample D18-4. The clot is ~5 mm in diameter and is a very coarse-grained aggregate of plagioclase with minor olivine and clinopyroxene. It closely resembles gabbroic clots described from ridges elsewhere [e.g., *Eaby et al.*, 1986; *Miller et al.*, 1994]. Its presence in type I lava, for which we later infer an important role of low-pressure fractional crystallization, may be significant, perhaps indi-

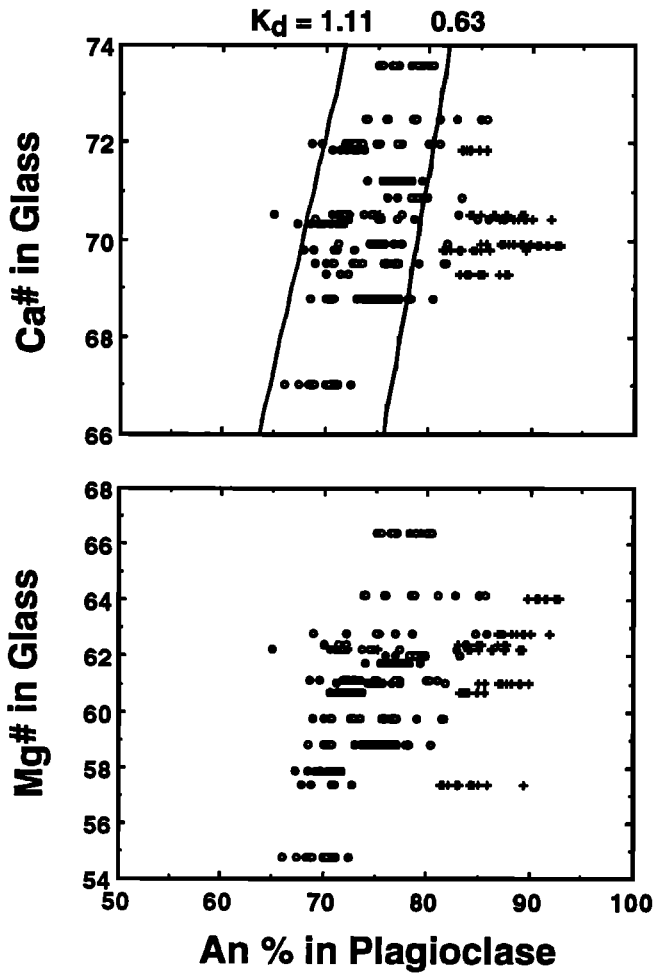

Figure 3. Plagioclase analyses plotted against Ca/(Ca+Na) and Mg/(Mg+Fe^{2+}) of their host glass. Circles are cores (solid) and rims (open) of phenocrysts. The crosses are megacrysts which display various resorption features (see text for discussion). No microlites are plotted, but they normally have low An contents and significant overlap with phenocrysts. For reference, we show K_d (Na-$Ca^{Pl\text{-}liq}$) values of 0.63 and 1.11. A large range of plagioclase-melt K_d has been observed previously [*Gerlach and Grove*, 1982]. Note (1) the large compositional variation, (2) the lack of systematic zoning relationships in phenocrysts (as a group) within single samples, and (3) very high An contents of megacrysts.

Table 3. Representative Probe Microanalyses of Plagioclase

	D14-1	D14-1	D15-2	D15-2	D15-4	D15-4	D15-4	D16-2	D16-2	D16-2	D16-2	D17-5	D17-5	D17-5	D18-4	D18-5	D18-5	D18-5	D18-5	D19-4	D19-4	D19-4	D20-4	D21-4
N	18	9	5	6	6	3	7	3	3	6	4	4	4	6	8	3	3	4	3	3	4	1	5	6
Grain	c	r	c	r	c	r	x	c	r	x	μ	c	r	x	clot	c	r	x-c	x-r	c	r	μ	x	c
SiO_2	50.18	50.45	51.29	51.52	51.37	51.02	47.72	50.87	51.11	47.67	50.72	49.91	49.25	46.70	49.06	51.51	50.39	47.16	50.39	49.42	49.50	51.96	45.94	48.91
Al_2O_3	31.25	31.13	29.99	30.34	30.06	30.75	33.00	30.79	30.68	33.25	31.15	31.27	31.69	34.32	31.45	30.22	30.98	33.65	30.98	31.74	31.77	29.72	34.52	32.44
FeO	0.43	0.43	0.48	0.56	0.52	0.64	0.33	0.52	0.45	0.31	0.55	0.43	0.41	0.28	0.56	0.56	0.45	0.37	0.50	0.39	0.44	0.77	0.27	0.43
MgO	0.25	0.23	0.25	0.25	0.28	0.25	0.19	0.31	0.26	0.21	0.26	0.23	0.23	0.19	0.25	0.25	0.26	0.16	0.25	0.26	0.24	0.44	0.19	0.39
CaO	14.82	14.77	14.13	14.07	13.98	14.23	16.61	14.44	14.25	16.76	14.19	15.15	15.33	17.43	15.25	14.41	14.88	16.99	14.45	15.44	15.62	13.84	18.17	15.02
Na_2O	2.87	2.98	3.29	3.32	3.26	3.29	1.92	3.18	3.17	1.82	3.17	2.86	2.65	1.51	2.86	3.29	2.97	1.72	3.03	2.66	2.53	3.55	1.17	2.49
K_2O	0.04	0.05	0.04	0.02	0.05	0.03	0.04	0.03	0.03	0.01	0.04	0.01	0.02	0.02	0.02	0.05	0.05	0.05	0.08	0.03	0.03	0.04	0.03	0.01
Sum	99.83	100.04	99.46	100.10	99.52	100.20	99.81	100.14	99.95	100.04	100.08	99.87	99.58	100.45	99.44	100.30	99.98	100.11	99.69	99.95	100.14	100.32	100.28	99.69
Si	2.294	2.302	2.349	2.344	2.350	2.323	2.194	2.317	2.329	2.187	2.310	2.284	2.262	2.138	2.258	2.342	2.302	2.165	2.306	2.262	2.262	2.361	2.112	2.241
Al	1.683	1.673	1.618	1.627	1.620	1.649	1.788	1.653	1.647	1.797	1.672	1.686	1.715	1.852	1.706	1.619	1.667	1.820	1.671	1.712	1.711	1.591	1.870	1.752
Fe^{3+}	0.023	0.025	0.033	0.029	0.030	0.028	0.018	0.030	0.024	0.016	0.018	0.029	0.023	0.010	0.033	0.038	0.031	0.014	0.023	0.026	0.028	0.047	0.018	0.010
Ca	0.726	0.722	0.693	0.686	0.685	0.694	0.818	0.704	0.696	0.823	0.692	0.743	0.754	0.855	0.752	0.702	0.728	0.835	0.709	0.757	0.764	0.674	0.894	0.737
Fe^{2+}	0.001	0.001	0.000	0.001	0.000	0.000	0.000	0.000	0.000	0.001	0.005	0.000	0.001	0.002	0.001	0.000	0.000	0.002	0.003	0.000	0.000	0.000	0.001	0.008
Mg	0.017	0.015	0.017	0.017	0.019	0.017	0.013	0.021	0.018	0.014	0.017	0.016	0.016	0.013	0.017	0.017	0.017	0.011	0.017	0.018	0.017	0.030	0.013	0.026
Na	0.254	0.263	0.292	0.293	0.289	0.291	0.171	0.281	0.280	0.162	0.280	0.254	0.235	0.134	0.256	0.290	0.263	0.153	0.269	0.236	0.224	0.313	0.104	0.221
K	0.002	0.003	0.002	0.001	0.003	0.002	0.002	0.002	0.002	0.001	0.003	0.001	0.001	0.001	0.001	0.003	0.003	0.003	0.005	0.002	0.002	0.002	0.002	0.001
Cations	5.000	5.004	5.004	4.998	4.996	5.003	5.005	5.007	4.995	5.001	4.997	5.013	5.008	5.005	5.026	5.011	5.011	5.004	5.002	5.013	5.007	5.019	5.014	4.996
An%	73.89	73.08	70.22	69.97	70.08	70.33	82.48	71.37	71.18	83.52	71.01	74.49	76.10	86.37	76.91	70.57	73.31	84.27	72.15	76.09	77.19	68.14	89.41	76.90
Or%	0.24	0.28	0.23	0.12	0.31	0.19	0.25	0.19	0.15	0.08	0.26	0.09	0.14	0.13	0.01	0.26	0.27	0.32	0.46	0.19	0.20	0.23	0.16	0.07

	D21-4	D21-4	D21-5	D21-5	D21-5	D21-6	D21-6	D21-6	D21-9	D21-9	D22-2	D22-2	D22-2	D23-6	D23-6	D23-6	D24-1	D24-1	D24-1	D24-1	D25-1	D25-1	D25-1	D25-1
N	4	4	5	3	4	8	6	4	7	2	5	8	5	11	8	4	2	2	9	3	3	2	9	3
Grain	r	μ	c	r	μ	c	r	μ	c	r	c	r	μ	c	r	μ	c	r	x	μ	c	r	x	μ
SiO_2	48.64	48.87	48.30	48.13	49.11	50.18	49.48	50.41	49.25	49.32	50.79	51.19	50.44	49.71	50.17	50.33	49.58	50.94	47.08	50.99	48.88	50.45	45.76	50.21
Al_2O_3	32.62	32.65	33.19	33.56	32.42	31.64	31.61	31.43	32.20	31.70	31.35	30.87	31.70	32.32	32.20	31.33	32.63	31.66	34.58	31.33	32.92	30.96	35.23	31.80
FeO	0.44	0.47	0.33	0.45	0.56	0.36	0.45	0.53	0.29	0.36	0.48	0.55	0.57	0.49	0.54	0.60	0.63	0.51	0.37	0.61	0.28	0.65	0.32	0.64
MgO	0.32	0.34	0.22	0.24	0.31	0.33	0.28	0.26	0.24	0.28	0.26	0.27	0.28	0.24	0.24	0.33	0.27	0.27	0.20	0.28	0.23	0.39	0.20	0.30
CaO	15.16	15.05	15.49	15.75	15.05	14.66	14.89	14.20	15.07	15.52	14.05	13.52	13.98	15.01	14.56	14.27	15.23	14.39	16.92	13.95	15.41	14.12	17.66	14.49
Na_2O	2.37	2.52	2.34	2.19	2.52	2.88	2.71	3.01	2.63	2.65	3.16	3.44	3.34	2.77	2.94	3.03	2.60	3.15	1.71	3.34	2.32	3.04	1.32	2.91
K_2O	0.03	0.06	0.03	0.04	0.04	0.03	0.03	0.03	0.03	0.02	0.03	0.04	0.02	0.04	0.03	0.04	0.00	0.03	0.01	0.03	0.02	0.00	0.01	0.03
Sum	99.60	99.96	99.90	100.35	100.01	100.09	99.46	99.88	99.72	99.85	100.13	99.88	100.33	100.57	100.69	99.93	100.96	100.95	100.87	100.52	100.06	99.62	100.50	100.38
Si	2.232	2.235	2.211	2.196	2.244	2.286	2.272	2.300	2.255	2.260	2.310	2.332	2.292	2.258	2.274	2.297	2.245	2.301	2.144	2.312	2.231	2.309	2.097	2.283
Al	1.764	1.759	1.790	1.805	1.746	1.699	1.710	1.690	1.737	1.712	1.680	1.657	1.698	1.730	1.720	1.685	1.742	1.685	1.856	1.673	1.771	1.669	1.903	1.704
Fe^{3+}	0.008	0.006	0.001	0.002	0.010	0.015	0.018	0.011	0.011	0.029	0.011	0.012	0.012	0.012	0.008	0.018	0.012	0.015	0.002	0.015	0.002	0.022	0.003	0.014
Ca	0.745	0.737	0.760	0.770	0.737	0.716	0.732	0.694	0.739	0.762	0.684	0.659	0.681	0.730	0.707	0.698	0.739	0.696	0.825	0.677	0.753	0.692	0.867	0.706
Fe^{2+}	0.011	0.012	0.011	0.015	0.011	0.003	0.003	0.010	0.006	0.000	0.009	0.009	0.010	0.007	0.014	0.008	0.012	0.004	0.012	0.008	0.009	0.011	0.010	0.011
Mg	0.022	0.023	0.015	0.017	0.021	0.022	0.019	0.018	0.017	0.019	0.018	0.019	0.019	0.016	0.016	0.022	0.018	0.018	0.014	0.019	0.016	0.027	0.013	0.020
Na	0.211	0.224	0.207	0.193	0.223	0.254	0.241	0.266	0.233	0.235	0.278	0.304	0.294	0.244	0.258	0.268	0.228	0.276	0.151	0.293	0.205	0.270	0.117	0.256
K	0.002	0.003	0.001	0.002	0.002	0.002	0.002	0.002	0.002	0.001	0.002	0.002	0.001	0.002	0.002	0.002	0.000	0.002	0.001	0.002	0.001	0.000	0.001	0.002
Cations	4.995	4.999	4.998	4.999	4.995	4.997	4.998	4.989	4.999	5.018	4.992	4.993	5.007	5.000	4.998	4.999	4.998	4.996	5.004	4.999	4.987	4.999	5.012	4.995
An%	77.79	76.44	78.44	79.75	76.57	73.66	75.06	72.15	75.91	76.30	70.95	68.31	69.74	74.78	73.16	72.10	76.42	71.46	84.47	69.64	78.51	71.93	87.99	73.23
Or%	0.19	0.36	0.15	0.22	0.25	0.19	0.20	0.19	0.17	0.11	0.18	0.22	0.11	0.25	0.17	0.24	0.00	0.20	0.08	0.20	0.13	0.00	0.09	0.20

N is number of analyses averaged; grain is c, core; r, rim; g, groundmass; x, very large phenocrysts (xenocrysts?); and clot, plagioclase of the crystal clot (see text for discussion). Fe^{3+} is obtained by stoichiometry. Note that the zoning, if it exists, is not systematic. Analyses were done at the University of Hawaii, Honolulu.

Table 4. Representative Probe Microanalyses of Quench Clinopyroxene

Sample	D14-1	D14-1	D14-1	D14-1	D14-1	D15-2	D15-2	D15-2	D15-2	D15-2	D15-2	D15-2	D15-2	D15-2
Grain	1	2	3	4	5	1	2	3	4	5	6	7	8	9
Point	3	5	5	3	6	5	2	3	4	2	1	11	10	5
SiO_2	52.61	52.46	53.47	52.65	52.48	52.1	52.92	53.14	53.41	52.25	52.71	52.75	51.66	51.86
TiO_2	0.48	0.57	0.41	0.49	0.53	0.58	0.51	0.65	0.36	0.65	0.45	0.52	0.78	0.70
Al_2O_3	3.09	3.49	2.41	3.05	3.22	3.62	3.10	3.14	2.19	3.56	2.31	2.98	4.24	4.16
Cr_2O_3	0.41	0.35	0.36	0.28	0.50	0.53	0.57	0.44	0.52	0.76	0.45	0.00	0.00	0.00
FeOt	5.95	6.08	6.21	6.12	6.08	5.78	5.84	6.61	5.41	5.51	5.66	6.01	5.74	6.02
MnO	0.10	0.14	0.14	0.06	0.12	0.12	0.07	0.09	0.12	0.10	0.21	0.20	0.19	0.16
MgO	18.35	18.62	19.72	18.51	19.36	18.21	18.53	19.75	19.53	18.18	18.55	18.57	17.27	17.34
CaO	18.92	18.45	17.61	18.69	17.73	19.11	19.05	17.52	18.83	19.75	19.36	18.58	19.66	19.04
Na_2O	0.26	0.26	0.19	0.26	0.22	0.25	0.22	0.22	0.23	0.30	0.27	0.23	0.28	0.28
Total	100.16	100.43	100.51	100.11	100.24	100.3	100.8	101.56	100.6	101.05	99.96	99.84	99.85	99.58
Si	1.915	1.904	1.933	1.917	1.905	1.896	1.914	1.905	1.931	1.890	1.926	1.924	1.890	1.900
Ti	0.013	0.016	0.011	0.013	0.014	0.016	0.014	0.018	0.01	0.018	0.012	0.014	0.021	0.019
Al	0.133	0.149	0.103	0.131	0.138	0.155	0.132	0.133	0.093	0.152	0.099	0.128	0.183	0.180
Cr	0.012	0.010	0.010	0.008	0.014	0.015	0.016	0.013	0.015	0.022	0.013	-	-	-
Fe^{2+}	0.181	0.184	0.187	0.186	0.184	0.176	0.176	0.198	0.163	0.166	0.173	0.183	0.175	0.184
Mn	0.003	0.004	0.004	0.002	0.004	0.004	0.002	0.003	0.004	0.003	0.006	0.006	0.006	0.005
Mg	0.995	1.007	1.062	1.004	1.047	0.987	0.998	1.053	1.052	0.980	1.009	1.009	0.941	0.946
Ca	0.738	0.717	0.682	0.729	0.689	0.745	0.738	0.674	0.730	0.765	0.757	0.726	0.770	0.747
Na	0.018	0.019	0.013	0.018	0.015	0.017	0.015	0.016	0.016	0.021	0.019	0.016	0.020	0.020
ΣCations	4.008	4.010	4.006	4.009	4.012	4.011	4.006	4.012	4.013	4.016	4.015	4.006	4.008	4.001
En	0.519	0.526	0.548	0.523	0.544	0.516	0.521	0.546	0.54	0.512	0.519	0.524	0.497	0.502
Wo	0.385	0.375	0.353	0.379	0.359	0.39	0.385	0.351	0.375	0.4	0.389	0.378	0.407	0.397
Fs	0.096	0.099	0.099	0.098	0.098	0.094	0.093	0.104	0.086	0.089	0.092	0.098	0.096	0.101

Sample	D15-4	D15-4	D15-4	D15-4	D15-4	D15-4	D16-2	D16-2	D22-2	D22-4	D22-4	D22-4	D22-4
Grain	1	2	3	4	5	6	6	7	1	1	2	3	4
Point	4	4	3	2	2	5	7	5	3	4	2	5	7
SiO_2	52.52	53.43	52.24	53.03	53.26	51.99	50.99	51.41	52.83	52.42	52.17	52.14	52.32
TiO_2	0.52	0.40	0.51	0.40	0.45	0.62	0.84	0.79	0.55	0.59	0.61	0.70	0.62
Al_2O_3	3.27	2.21	3.19	2.53	2.64	3.85	4.50	4.44	3.30	3.66	3.96	3.90	3.57
Cr_2O_3	0.59	0.47	0.53	0.53	0.49	0.48	0.00	0.00	0.24	0.48	0.72	0.30	0.47
FeOt	5.62	6.10	5.77	5.90	5.87	5.63	5.45	5.44	6.91	6.01	5.88	6.47	6.02
MnO	0.10	0.11	0.10	0.21	0.16	0.11	0.16	0.15	0.16	0.13	0.14	0.14	0.15
MgO	18.78	20.05	18.49	19.28	19.71	18.8	17.21	17.56	16.87	17.87	18.11	16.85	18.19
CaO	18.72	17.48	18.87	18.32	17.86	18.66	19.76	19.46	19.13	19.37	18.86	19.65	19.08
Na_2O	0.19	0.17	0.19	0.24	0.19	0.24	0.28	0.29	0.25	0.27	0.28	0.28	0.25
Total	100.31	100.42	99.89	100.44	100.63	100.38	99.22	99.55	100.23	100.8	100.75	100.43	100.67
Si	1.906	1.933	1.907	1.923	1.923	1.887	1.877	1.883	1.928	1.900	1.890	1.902	1.898
Ti	0.014	0.011	0.014	0.011	0.012	0.017	0.023	0.022	0.015	0.016	0.017	0.019	0.017
Al	0.140	0.095	0.137	0.108	0.113	0.165	0.195	0.192	0.142	0.156	0.169	0.167	0.153
Cr	0.017	0.013	0.015	0.015	0.014	0.014	-	-	0.007	0.014	0.021	0.009	0.014
Fe^{2+}	0.170	0.184	0.176	0.179	0.177	0.171	0.168	0.166	0.211	0.182	0.178	0.197	0.182
Mn	0.003	0.003	0.003	0.006	0.005	0.003	0.005	0.005	0.005	0.004	0.004	0.004	0.004
Mg	1.015	1.079	1.005	1.042	1.060	1.016	0.944	0.958	0.917	0.965	0.977	0.915	0.983
Ca	0.728	0.678	0.738	0.712	0.691	0.726	0.779	0.763	0.748	0.752	0.732	0.768	0.742
Na	0.014	0.012	0.013	0.017	0.013	0.017	0.020	0.021	0.017	0.019	0.020	0.020	0.018
ΣCations	4.008	4.008	4.009	4.013	4.008	4.015	4.013	4.010	3.991	4.008	4.008	4.001	4.011
En	0.529	0.555	0.523	0.537	0.548	0.530	0.498	0.506	0.488	0.507	0.517	0.486	0.514
Wo	0.380	0.349	0.384	0.368	0.358	0.379	0.411	0.403	0.398	0.395	0.387	0.408	0.388
Fs	0.090	0.096	0.093	0.095	0.094	0.091	0.091	0.090	0.115	0.098	0.096	0.107	0.098

Analyses were done at the University of Hawaii, Honolulu.

cating that fractionation occurred in a mush-rich chamber of the sort discussed by *Sinton and Detrick* [1992].

Basalt Chemistry

Basalt glasses were analyzed using the electron microprobe at the Smithsonian Institution, Washington, D. C. (T. O'Hearn, analyst) for major elements and representative analyses are given in Table 5. Additional representative whole rock major element analyses were done by XRF at the University of Hawaii, Honolulu (Table 6), with trace elements by XRF (University of Hawaii), Instrumental Neutron Activation Analysis (INAA, at Washington University, St.

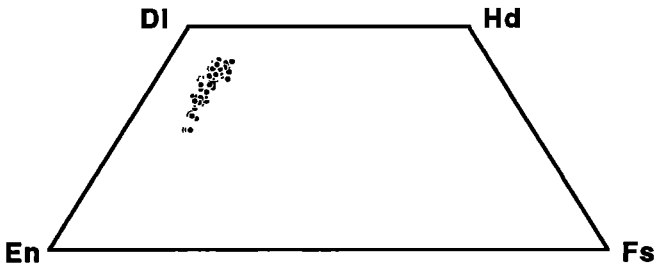

Figure 4. Quench clinopyroxene analyses plotted in the pyroxene quadrilateral. The very tight trend subparallel to the Di-En join indicates that all these clinopyroxene crystals have very similar $Mg^{\#}$, but variable amount of CaO or Wo component. They show little correlation with the chemistry of their host melt, implying that cooling rate may have been an important factor controlling their chemistry [*Grove and Bryan*, 1983].

Louis), and DCP (plasma atomic emission spectroscopy) at Northwestern University, Evanston. In Table 6, for trace elements, we show only the INAA data and a few XRF analyses for representative samples; however, all the additional trace element analyses and XRF major element analyses are available from the authors or as electronic supplement.[1] A detailed comparison of the XRF major element whole rock and probe analyses of glass indicates that the two techniques yield very similar results for aphyric samples. As expected, whole rock analyses of phyric samples differ to various extents from probe analyses of glass, reflecting the effects of the added solid phases. For this reason, we restrict ourselves to glass analyses in our discussion of the major elements.

Major elements. The samples from 26°S MAR are exclusively normal, depleted mid-ocean ridge basalts (N-MORB) (see Tables 5 and 6). The glasses range in composition from relatively primitive (MgO = 8.62 wt %) to moderately evolved (MgO = 6.55 wt %), and show considerable scatter on MgO variation diagrams (Figure 5). Type I samples (plagioclase first) tend to have similar Al_2O_3, higher CaO, and lower FeO, TiO_2, and Na_2O at the same MgO content, than type II (olivine first) samples (Figure 5). Type I samples also define fairly simple curvilinear trends on MgO variation diagrams and include the most evolved samples from the segment. In contrast, type II samples show much more chemical variability and scatter on MgO variation diagrams (Figure 5).

Figure 6 shows the along-axis variation of MgO and Al_2O_3, which along with the other major elements, define rough W- or M-shaped patterns. Lavas with relatively high eruption temperatures (Figure 6) are found at the ends of the segment near the offsets (type II) and also near the top of the central high (types I and II). Interestingly, however, the lavas with the highest eruption temperatures are found not at the top of the central high but rather about halfway down its southern slope in a dredge haul (D 21) also containing moderately evolved basalts. Figure 6 thus shows that the correspondence among basalt types (types I and II), basalt chemistry, and tectonic occurrence (central high, near offsets and in-between) is imperfect. Nevertheless, it is true that closest to the offsets, our sampling recovered only relatively primitive, type II basalts. Further, MgO generally decreases away from the offsets and rises again (with scatter) in the central part of the segment.

As shown in Figure 7, the type I basalts occurring away from offsets appear to comprise a coherent fractionation sequence on the basis of both least squares mixing calculations [*Bryan*, 1986] and the liquid-line-of-descent model of *Weaver and Langmuir* [1990]. Despite the apparent success of this model, we interpret these results with caution for several reasons. First, the samples considered are dispersed along more than 75 km of ridge axis, so it is unlikely that the samples comprise, literally, a fractionation series. More importantly, the available trace element data do not favor the hypothesis that all type I samples are related by simple fractional crystallization. Furthermore, as we show below, the major oxides corrected for fractionation to 8 wt % MgO indicate that melts throughout the segment are derived by melting under individually distinct conditions. Thus, while it is clear that many of the melts, particularly those of type I, have undergone fractionation of low-pressure phase assemblages, their parental melts are not identical. Taken together, type I and type II melts represent a wide range of parental melts produced by melting under diverse conditions.

Evidence for differences in parental melt compositions throughout the segment may be seen in Figure 8, showing several oxides and oxide ratios normalized to MgO values of 8 wt % [*Klein and Langmuir*, 1987]. The correction method we used [from *Niu*, 1992] is described in Table 7. Except for $Al_{[8]}$ and $Na_{[8]}$, whose variations are below the level of analytical uncertainty, the normalized oxides show smoothed along-axis variation patterns that are either symmetrical or slightly skewed. Following the interpretations of *Niu and Batiza* [1991a], the patterns of $Ti_{[8]}$, $Ca_{[8]}$, and $Ca_{[8]}/Al_{[8]}$ indicate lower extents of melting near the offsets with increased extents of melting toward the center of the segment. Similarly, $Si_{[8]}$, $Fe_{[8]}$, and $Si_{[8]}/Fe_{[8]}$ are indicative of deeper melting near the offsets, with shallower melting toward the center of the segment.

In order to quantify these estimates of the extent and depth of melting, we use equations (8)–(10) of *Niu and Batiza* [1991a]. For this application, we have modified the equations slightly to exclude Na_2O and Al_2O_3 from calculations of the extent of melting (F) because as we show later, there is reason to believe that the levels of these elements in the mantle source of the 26°S lavas is anomalous relative to the abundances of TiO_2, CaO, FeO, and the other major oxides. The results shown in Figure 9 indicate that the extent of melting varies from about 15% to 18%. Our computed depths of initial melting (P_o) are essentially constant at ~16 kbar, indicating that the observed differences in $Si_{[8]}/Fe_{[8]}$ are most likely due to the effects of F on this ratio [*Niu and Batiza*, 1991a]. Even though P_o is constant, the computed depth of final melting (P_f) varies from ~12 kbar near the offsets to ~10 kbar in the middle of the segment. This is because of the calculated variations in F and the way in which P_f is defined by *Niu and Batiza* [1991a]. Interestingly, the pattern we calculate for variations in F shows

[1]An electronic supplement of this material may be obtained on a diskette or Anonymous FTP from KOSMOS.AGU.ORG. (LOGIN to AGU's FTP account using ANONYMOUS as the username and GUEST as the password. Go to the right directory by typing CD APEND. Type LS to see what files are available. Type GET and the name of the file to get it. Finally, type EXIT to leave the system.) (Paper 94JB01663, Magmatic processes at a slow spreading ridge segment: 26°S Mid-Atlantic Ridge, by Y. Niu and R. Batiza). Diskette may be ordered from American Geophysical Union, 2000 Florida Avenue, N.W., Washington, DC 20009; $15.00. Payment must accompany order.

a maximum located slightly north of the middle of the segment, like the pattern of along-axis topography (Figure 6), although it is not clear whether this is significantly different from the symmetrical line drawn through the data in Figure 9.

Trace elements. Trace element data are given in Table 6. On MgO variation diagrams (not shown) the compatible trace elements (e.g., Ni and Cr) show scattered but reasonably positive correlation with MgO. In contrast, the strongly and moderately incompatible elements show more scatter and much poorer correlations, even for type I samples alone. The trace element data thus do not support the simple fractional crystallization hypothesis for type I basalts discussed previously. The observed noisy trace element patterns are probably at least partly the result of mantle heterogeneity; however, the absolute level of this heterogeneity is small, as shown by the narrow ranges of $[La/Sm]_N$ (0.468 to 0.596), $[Ce/Yb]_N$ (0.741 to 0.896), and other trace element ratios.

It is interesting that despite the small variations in these

Table 5. Probe Microanalyses of MAR Basaltic Glasses

	D12-2A	D12-2B	D12-2sh	D12-3sh	D12-4	D12-6	D12-7	D12-10	D12-19	D12-20	D12-21	D12-23	D12-24
SiO_2	50.84	50.59	50.82	51.61	50.42	50.88	50.64	50.42	50.30	51.01	50.66	50.82	50.82
TiO_2	1.65	1.60	1.61	1.67	1.70	1.70	1.62	1.71	1.66	1.70	1.69	1.65	1.68
Al_2O_3	15.43	15.30	15.30	15.36	15.26	15.19	15.42	15.46	15.18	15.45	15.30	15.38	15.32
FeOt	9.92	9.92	9.86	9.75	9.96	9.87	9.96	10.02	9.98	9.50	9.98	9.75	9.40
MgO	8.01	8.09	7.96	7.78	8.08	7.66	8.05	7.51	8.16	7.80	7.97	8.02	7.61
CaO	11.04	11.09	11.27	11.41	11.04	11.41	11.16	11.65	11.04	11.42	11.18	11.34	11.37
Na_2O	2.73	2.65	2.70	2.30	2.75	2.72	2.70	2.60	2.72	2.72	2.71	2.72	2.63
K_2O	0.09	0.10	0.09	0.09	0.11	0.08	0.09	0.08	0.10	0.09	0.08	0.10	0.10
P_2O_5	0.18	0.16	0.16	0.17	0.14	0.16	0.14	0.14	0.16	0.17	0.16	0.18	0.12
Total	99.89	99.50	99.77	100.14	99.46	99.67	99.78	99.59	99.30	99.86	99.73	99.96	99.05
Mg#	61.53	61.76	61.52	61.25	61.64	60.59	61.55	59.75	61.82	61.92	61.27	61.97	61.59

	D12-26	D12-29	D12-30	D12-30	D12-32	D12-33	D12-36	D12-37	D13-1	D13-2	D13-3	D13-4	D13-5
SiO_2	50.83	50.37	50.27	50.35	50.39	50.22	51.03	50.68	50.56	50.72	50.63	51.29	51.45
TiO_2	1.59	1.60	1.58	1.63	1.62	1.64	1.71	1.60	1.53	1.55	1.57	1.59	1.58
Al_2O_3	15.43	15.35	15.32	15.14	15.22	15.29	15.07	15.30	15.20	15.31	14.97	15.59	15.42
FeOt	9.55	9.72	9.82	10.08	9.95	10.10	10.03	9.70	9.91	9.64	9.62	9.75	9.57
MgO	7.85	8.22	8.07	8.04	8.25	8.04	7.57	8.06	7.88	7.89	7.70	7.91	7.78
CaO	11.34	11.24	11.10	11.02	11.10	10.97	11.37	11.34	11.46	11.52	11.62	11.39	11.47
Na_2O	2.69	2.72	2.63	2.76	2.74	2.69	2.71	2.75	2.67	2.64	2.67	2.68	2.60
K_2O	0.08	0.10	0.09	0.08	0.10	0.08	0.09	0.08	0.08	0.08	0.10	0.09	0.09
P_2O_5	0.16	0.12	0.15	0.17	0.14	0.13	0.17	0.16	0.14	0.15	0.13	0.15	0.16
Total	99.52	99.44	99.03	99.27	99.51	99.16	99.75	99.67	99.43	99.50	99.01	100.44	100.12
$Mg^{\#}$	61.95	62.62	61.94	61.24	62.15	61.19	59.92	62.20	61.16	61.85	61.32	61.64	61.69

	D13-6	D13-7	D13-8	D13-9	D13-10	D13-11	D14-1	D14-2	D15-1	D15-2	D15-3	D15-4	D15-5
SiO_2	51.00	50.61	51.20	50.93	50.78	51.03	51.36	51.22	51.02	51.63	51.25	51.68	51.41
TiO_2	1.61	1.58	1.61	1.59	1.59	1.62	1.57	1.56	1.53	1.51	1.53	1.54	1.54
Al_2O_3	15.41	15.49	15.60	15.47	15.59	15.42	14.76	14.68	14.67	14.61	14.75	14.60	14.65
FeOt	9.79	9.86	9.62	9.70	9.68	9.71	9.77	10.06	10.29	10.29	10.35	10.13	10.20
MgO	7.63	7.76	7.70	7.66	7.64	7.67	7.05	7.14	7.14	7.14	7.07	6.88	7.04
CaO	11.42	11.33	11.46	11.29	11.40	11.51	11.76	11.74	11.80	11.88	11.86	11.95	11.70
Na_2O	2.65	2.58	2.67	2.63	2.63	2.68	2.94	2.82	2.85	2.76	2.82	2.85	2.85
K_2O	0.10	0.08	0.09	0.08	0.07	0.09	0.06	0.08	0.07	0.07	0.05	0.07	0.06
P_2O_5	0.14	0.14	0.13	0.11	0.16	0.12	0.12	0.15	0.14	0.17	0.17	0.17	0.15
Total	99.75	99.43	100.08	99.46	99.54	99.85	99.39	99.45	99.51	100.06	99.85	99.87	99.60
$Mg^{\#}$	60.69	60.92	61.32	61.00	60.99	61.01	58.83	58.43	57.88	57.88	57.50	57.36	57.75

	D15-6	D16-1	D16-2	D17-1	D17-3	D17-4	D17-5	D17-6	D17-7	D18-1	D18-2	D18-3	D18-4
SiO_2	51.12	51.70	51.26	51.10	51.18	50.76	50.95	51.24	50.96	50.90	50.82	51.25	50.84
TiO_2	1.50	1.35	1.38	1.41	1.37	1.39	1.38	1.41	1.38	1.31	1.33	1.34	1.35
Al_2O_3	14.50	15.05	15.00	15.24	15.31	14.95	15.12	14.94	15.12	15.42	15.53	15.36	15.54
FeOt	10.34	9.77	9.48	9.32	9.34	9.82	9.46	9.74	9.74	9.08	9.01	9.04	8.92
MgO	7.13	7.58	7.39	7.15	7.13	7.45	7.48	7.42	7.40	7.78	7.76	7.81	7.71
CaO	11.68	12.16	12.24	11.99	12.01	12.08	12.02	12.06	12.07	12.32	12.20	12.32	12.18
Na_2O	2.84	2.60	2.64	2.84	2.83	2.78	2.85	2.77	2.76	2.87	2.75	2.78	2.78
K_2O	0.06	0.04	0.04	0.07	0.08	0.07	0.09	0.08	0.07	0.08	0.06	0.08	0.08
P_2O_5	0.13	0.15	0.13	0.13	0.19	0.11	0.12	0.11	0.11	0.12	0.12	0.12	0.11
Total	99.30	100.40	99.56	99.25	99.44	99.41	99.47	99.77	99.61	99.88	99.58	100.10	99.51
$Mg^{\#}$	57.73	60.58	60.69	60.31	60.19	60.04	61.03	60.14	60.08	62.92	63.04	63.12	63.13

Table 5. (continued)

	D18-5	D19-1	D19-2	D19-3	D19-4	D19-5	D19-6	D19-7	D19-8	D19-9	D20-1	D20-2	D20-3
SiO_2	50.92	51.18	50.38	50.60	51.26	50.78	51.31	51.22	51.13	51.21	51.12	50.73	51.24
TiO_2	1.30	1.18	1.23	1.16	1.21	1.17	1.18	1.19	1.14	1.21	1.38	1.40	1.41
Al_2O_3	15.41	15.52	15.32	15.42	15.38	15.52	15.51	15.52	15.67	15.41	16.16	16.03	16.06
FeOt	9.14	8.80	8.82	8.92	8.87	8.81	9.02	8.73	8.71	8.78	9.12	9.26	9.07
MgO	7.71	8.16	8.08	8.10	8.02	8.15	8.12	8.18	8.07	8.13	8.06	8.01	8.02
CaO	12.25	12.25	12.25	12.18	12.20	12.24	12.23	12.24	12.24	12.30	11.63	11.54	11.48
Na_2O	2.82	2.63	2.56	2.56	2.55	2.58	2.44	2.64	2.61	2.57	2.70	2.69	2.73
K_2O	0.08	0.08	0.06	0.07	0.06	0.07	0.07	0.07	0.08	0.06	0.08	0.07	0.08
P_2O_5	0.12	0.11	0.14	0.12	0.14	0.14	0.13	0.12	0.10	0.13	0.14	0.15	0.12
Total	99.75	99.91	98.84	99.13	99.69	99.46	100.01	99.91	99.75	99.80	100.39	99.88	100.21
$Mg^{\#}$	62.56	64.75	64.47	64.27	64.17	64.69	64.07	64.98	64.73	64.71	63.64	63.14	63.65

	D20-4	D21-1	D21-2	D21-3	D21-4	D21-5	D21-6	D21-8	D21-9	D22-1	D22-2	D22-3	D22-5
SiO_2	50.88	51.40	50.93	51.31	50.61	51.63	51.61	50.68	51.43	51.66	51.42	51.50	51.62
TiO_2	1.38	1.53	1.14	1.12	1.09	1.27	1.50	1.10	1.31	1.45	1.73	1.46	1.80
Al_2O_3	16.02	14.77	16.00	15.84	16.16	15.14	14.97	16.23	15.01	14.52	14.21	14.50	14.30
FeOt	8.98	9.70	8.66	8.75	8.64	9.24	9.58	8.54	9.08	9.83	10.93	9.92	11.06
MgO	8.09	7.50	8.49	8.55	8.62	7.62	7.61	8.40	7.39	7.00	6.69	7.01	6.62
CaO	11.58	12.16	12.44	12.33	12.25	12.32	12.13	12.34	12.27	11.75	11.07	11.78	11.13
Na_2O	2.75	2.63	2.41	2.44	2.42	2.79	2.60	2.39	2.73	2.85	3.00	2.95	3.02
K_2O	0.08	0.08	0.05	0.04	0.05	0.08	0.07	0.06	0.06	0.08	0.07	0.09	0.08
P_2O_5	0.14	0.16	0.12	0.10	0.10	0.14	0.16	0.11	0.12	0.14	0.13	0.17	0.16
Total	99.90	99.93	100.24	100.48	99.94	100.23	100.23	99.85	99.40	99.28	99.25	99.38	99.79
$Mg^{\#}$	64.09	60.50	66.01	65.93	66.40	62.03	61.14	66.08	61.72	58.51	54.80	58.33	54.24

	D22-6	D22-7	D22-8	D22-9	D22-10	D23-1	D23-2	D23-3	D23-4	D23-5	D23-6	D23-7	D23-8
SiO_2	51.75	51.95	51.51	51.42	51.42	50.62	50.76	51.01	50.63	50.74	50.59	50.65	50.59
TiO_2	1.26	1.78	1.74	1.75	1.73	1.72	1.70	1.73	1.70	1.71	1.74	1.66	1.68
Al_2O_3	14.97	14.32	14.24	14.20	14.26	15.43	15.18	15.29	15.26	15.16	15.30	15.24	15.26
FeOt	9.21	10.76	10.69	10.88	11.02	9.85	9.80	9.73	9.91	9.89	10.17	9.80	9.88
MgO	7.52	6.67	6.68	6.58	6.55	7.37	7.29	7.38	7.54	7.54	7.62	7.56	7.53
CaO	12.44	11.21	11.26	11.14	11.16	11.42	11.43	11.34	11.46	11.30	11.38	11.46	11.48
Na_2O	2.58	2.93	2.89	2.96	2.96	2.78	2.71	2.71	2.71	2.78	2.75	2.72	2.69
K_2O	0.07	0.07	0.10	0.09	0.07	0.10	0.08	0.08	0.09	0.08	0.09	0.09	0.08
P_2O_5	0.11	0.16	0.16	0.18	0.15	0.17	0.19	0.20	0.16	0.18	0.22	0.18	0.15
Total	99.91	99.85	99.27	99.20	99.32	99.46	99.14	99.47	99.46	99.38	99.86	99.36	99.34
$Mg^{\#}$	61.79	55.11	55.31	54.50	54.07	59.71	59.57	60.04	60.11	60.16	59.74	60.44	60.15

	D24-1	D24-2	D25-1	D26-1	D27-1	D27-2	D27-3	D27-4	D27-5	D27-6
SiO_2	50.86	51.10	50.06	50.70	50.94	50.70	50.76	50.97	50.93	50.78
TiO_2	1.54	1.54	1.41	1.43	1.41	1.43	1.38	1.41	1.43	1.41
Al_2O_3	15.49	15.58	15.74	15.39	15.85	15.57	15.49	15.43	15.57	15.74
FeOt	9.54	9.02	9.48	9.10	9.14	9.07	9.39	9.25	9.24	9.26
MgO	8.00	7.81	8.08	7.61	8.08	8.23	8.23	8.16	8.12	8.20
CaO	11.51	11.69	11.68	11.94	11.79	11.79	11.72	11.78	11.75	11.78
Na_2O	2.81	2.72	2.70	2.63	2.40	2.42	2.43	2.41	2.48	2.44
K_2O	0.07	0.06	0.06	0.06	0.07	0.07	0.07	0.08	0.07	0.08
P_2O_5	0.16	0.17	0.17	0.10	0.12	0.12	0.11	0.10	0.11	0.14
Total	99.98	99.69	99.38	98.96	99.80	99.40	99.58	99.59	99.70	99.83
$Mg^{\#}$	62.42	63.17	62.80	62.35	63.65	64.25	63.45	63.60	63.51	63.69

Analyses were done at the Smithsonian Institution. FeOt, total iron is expressed as FeO. $Mg^{\#} = Mg/(Mg + Fe^{2+})$, with $Fe^{2+}/(Fe^{2+} + Fe^{3+}) = 0.9$ assumed.

ratios, along-axis variation in these ratios shows a rough "W" pattern like the major elements (Figure 10). Ni also shows a crude "W" pattern, but the central peak is muted, and there is some scatter (Figure 10). Abundances of the rare earths (Figure 10) show crude U-shaped patterns, even for abundances normalized to 8 wt % MgO (Figure 11), in qualitative agreement with the expectations for melting of a homogeneous source to the extent inferred from the major elements (Figure 9) (i.e., less melting at the offsets, more melting in the middle of the segment). Quantitatively, however, this hypothesis fails, as the trace element abundances vary by 25% to 50% (Figures 10 and 11), whereas the inferred differences in the extent of

Table 6. Whole Rock Major and Trace Element Chemistry of Representative Samples

	D12-4	D12-23	D13-1	D13-6	D13-7	D14-2†	D15-1	D16-1†	D17-3†	D18-5	D19-1
SiO_2	50.20	50.09	50.60	50.47	51.13	50.80	50.69	50.70	50.49	50.90	50.64
TiO_2	1.66	1.60	1.59	1.59	1.59	1.38	1.39	1.28	1.36	1.30	1.21
Al_2O_3	14.92	14.95	15.03	15.02	15.25	14.89	14.68	15.04	17.16	15.34	15.27
FeOt	9.59	9.69	9.72	9.76	9.83	9.26	9.48	8.94	9.04	8.95	8.71
MnO	0.17	0.17	0.17	0.17	0.17	0.16	0.17	0.16	0.16	0.16	0.15
MgO	8.13	8.23	8.29	8.23	8.35	7.55	7.51	7.85	7.46	7.85	8.00
CaO	10.75	10.90	11.20	11.23	11.30	11.69	11.73	11.98	11.86	11.90	12.02
Na_2O	2.65	2.62	2.40	2.34	2.61	2.65	2.69	2.57	2.69	2.72	2.53
K_2O	0.10	0.10	0.08	0.07	0.07	0.04	0.06	0.03	0.12	0.06	0.05
P_2O_5	0.16	0.15	0.14	0.14	0.14	0.11	0.11	0.10	0.11	0.11	0.10
Total	98.85	99.02	99.70	99.47	100.97	99.07	99.06	77.17	100.98	99.84	99.18
$Mg^{\#}$	62.69	62.74	62.82	62.56	62.73	61.78	61.10	63.49	62.03	63.47	64.53
La	3.52	3.40	3.06	3.16	3.18		2.31			2.58	2.23
Ce	11.10	11.10	11.60	11.40	11.70		8.30			8.80	7.70
Sm	3.82	3.69	3.65	3.70	3.69		3.19			2.99	2.69
Eu	1.39	1.30	1.34	1.34	1.34		1.19			1.13	1.03
Tb	0.95	0.89	0.93	0.93	0.95		0.83			0.71	0.69
Yb	3.68	3.44	3.53	3.55	3.56		3.11			2.82	2.71
Lu	0.56	0.49	0.54	0.54	0.49		0.46			0.38	0.39
Sc	37.9	37.2	38.0	38.1	38.0	48.0	41.1	44.4	46.8	39.4	39.3
Cr	311	322	352	349	350	227	197	384	362	347	385
Ni	130	150	120	120	130	77	70	76	67	70	71
Cu						72.4		82.9	83.3		
Zn						77.1		72.3	74.7		
Sr	55	130	110	170	130	112	80	103	119	100	110
Y						33.5		30.7	31.6		
Zr	120	160		130	170	91	110	79	91	140	110
Hf	3.01	2.84	2.89	2.93	2.82		2.33			2.21	2.00
Th	0.150			0.090	0.090						0.110
$[La/Sm]_N$	0.596	0.595	0.542	0.552	0.557		0.468			0.558	0.536
$[Ce/Yb]_N$	0.838	0.896	0.913	0.892	0.913		0.741			0.867	0.789
$[La/Lu]_N$	0.677	0.747	0.610	0.630	0.699		0.541			0.731	0.611

D19-2	D19-8	D21-5	D22-4	D23-4	D23-7	D23-8	D24-1	D25-1†	D27-1	D27-3	D27-5
50.63	50.61	51.13	51.54	50.64	50.61	50.56	50.63	50.50	50.39	50.68	50.34
1.20	1.19	1.27	1.46	1.69	1.67	1.67	1.54	1.41	1.43	1.43	1.40
15.34	15.31	15.19	14.94	15.31	15.29	15.30	15.63	16.02	15.24	15.39	15.25
8.64	8.65	8.96	9.66	9.86	9.86	9.86	9.31	9.10	9.35	9.45	9.34
0.15	0.16	0.16	0.17	0.17	0.17	0.17	0.16	0.16	0.17	0.16	0.16
8.04	8.10	7.83	7.60	7.56	7.53	7.55	7.85	8.10	8.84	8.92	8.89
12.01	12.02	11.97	11.78	11.32	11.32	11.31	11.41	11.54	11.42	11.40	11.34
2.44	2.49	2.64	2.65	2.53	2.62	2.60	2.55	2.47	2.43	2.34	2.33
0.08	0.06	0.05	0.08	0.12	0.11	0.10	0.07	0.07	0.06	0.07	0.07
0.11	0.10	0.10	0.11	0.15	0.14	0.14	0.13	0.13	0.12	0.12	0.12
99.11	99.17	99.82	100.50	99.85	99.84	99.77	99.77	99.97	99.91	100.40	99.68
64.83	64.98	63.39	60.90	60.29	60.19	60.25	62.54	63.80	65.19	65.15	65.34
2.20	2.09	2.40	2.27	3.31	3.22	3.21	2.92		2.81	2.83	2.78
7.90	7.20	8.60	8.00	11.70	11.10	11.10	10.70		10.00	9.50	9.70
2.67	2.64	2.85	2.95	3.86	3.87	3.85	3.52		3.19	3.28	3.23
1.04	1.03	1.13	1.08	1.41	1.38	1.39	1.28		1.14	1.16	1.19
0.66	0.71	0.72	0.78	0.97	0.95	0.94	0.87		0.78	0.84	0.76
2.65	2.67	2.80	2.85	3.84	3.73	3.73	3.31		3.19	3.18	3.16
0.38	0.35	0.38	0.43	0.53	0.55	0.57	0.47		0.46	0.45	0.46
38.4	38.5	39.5	34.8	39.4	39.0	38.8	36.8	43.3	36.6	36.9	37.1
378	381	283	329	294	294	290	353	370	462	473	479
100	51	140	140	110	100	110	120	145	180	200	210
							76.5				
							81.0				
110	150	120	130	60	120	110	130	114	120	90	130
							33.3				
	100		90	150	170	160	150	98	70	120	90

Table 6. (continued)

D19-2	D19-8	D21-5	D22-4	D23-4	D23-7	D23-8	D24-1	D25-1†	D27-1	D27-3	D27-5
1.98	2.01	2.17	2.24 0.090	2.99 0.073	3.16	2.97	2.78		2.41	2.53	2.58
0.533	0.512	0.544	0.497	0.554	0.538	0.539	0.536		0.569	0.558	0.556
0.828	0.749	0.853	0.780	0.846	0.827	0.827	0.898		0.871	0.830	0.853
0.624	0.643	0.680	0.570	0.670	0.627	0.607	0.669		0.659	0.677	0.648

Major element (wt %) analyses were done by XRF at the University of Hawaii. Total Fe is expressed as FeOt. $Mg^{\#}$ = $Mg/(Mg + Fe^{2+})$, with $Fe^{2+}/(Fe^{2+} + Fe^{3+}) = 0.9$ assumed. Trace elements (in ppm) were analyzed by INA analysis at Washington University, St. Louis, Missouri [*Lindstrom and Korotev*, 1982]. Analytical precision is computed for each sample, and these vary slightly. Typical uncertainties (2σ) are La and Sm, 4%; Eu and Lu, 6%; Ce, 7%; Hf, 9%; Sc, 1.2 ppm; Cr, 10 ppm; Ni, 30 ppm; Zr, 50 ppm; Th, 0.04 ppm. The subscript N refers to ratios of those elements normalized to the primitive mantle of *Sun and McDonough* [1989].

†Trace elements analyses were done by XRF at the University of Hawaii [see *Mahoney et al.*, 1994].

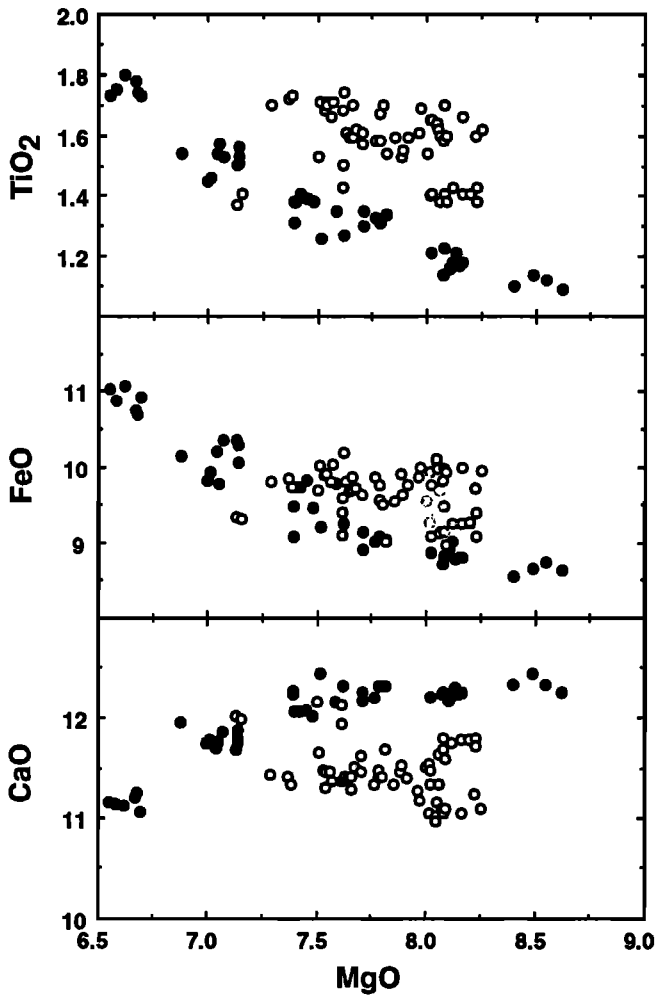

Figure 5. TiO_2, FeO, and CaO plotted against MgO of glass analyses, showing that the lavas from the entire ridge segment cannot be related by a common liquid line of descent, in contrast to N-MORB commonly observed for ridge segments at the EPR. We have divided the samples by petrographic type into type I and type II (see text for discussion of the differences). Type I lavas are shown by solid dots and may be related by a common liquid line of descent. Samples of this group are mostly from the interior of the segment. Type II lavas (open circles), mostly from near offsets, show much smaller MgO variation but large variations in TiO_2, FeO, and CaO.

melting are only on the order of 15% (Figure 9). Together, these somewhat contradictory observations lead us to conclude that the mantle source below the 26°S segment may be heterogeneous, leading to poor fits of the data to simple melting and fractionation hypotheses. However, the magnitude of the heterogeneity is probably small and may be linked to the major element composition of the source, as shown by the small observed variation in trace element ratios and their crude W-shaped along-axis variation patterns.

Isotopes. Isotopic data for Sr, Nd, Pb, and He (P. R. Castillo and D. W. Graham, manuscript in preparation, 1994) are in the range of normal MORB unaffected by plume components. However, small but significant variations do exist for both $^{87}Sr/^{86}Sr$ (0.702505 – 0.702589) and $^{143}Nd/^{144}Nd$ (0.513076 – 0.513140), and along-axis variations display rough W- and M-shaped patterns, respectively, like those for $[La/Sm]_N$ and $[Ce/Yb]_N$. The ratio $^3He/^4He$ also displays small but significant variation (R/R_A=7.32 – 7.73), and correlates well with $^{87}Sr/^{86}Sr$ (r^2 = 0.99) (D. W. Graham, personal communication, 1993). Instead of a "W" pattern, $^3He/^4He$ variations describe a U-shaped pattern like those of the REE abundances. A full discussion of the isotopic results is beyond the scope of this study, however the data do indicate that the mantle source below the 26°S segment is somewhat heterogeneous isotopically. In addition, the isotope data confirm the conclusion based on major and trace elements that the 26°S segment is fed by discrete melt batches with distinct petrogenetic histories.

Discussion

Cooling and Crystallization

It is well established that low-pressure cooling and fractionation are important processes affecting the chemistry of virtually all MORB lavas [e.g., *Walker et al.*, 1979]. Strong arguments have also been made for the importance of fractionation at higher pressure [e.g., *O'Hara*, 1965; *Elthon et al.*, 1982; *Elthon*, 1987; *Tormey et al.*, 1987; *Kinzler and Grove*, 1992; *Grove et al.*, 1992]. In this section, we consider the evidence in the 26°S lavas for fractionation at various pressures, the potential sites of cooling and fractionation and implications for along-axis chemical variations and magma supply geometry.

The petrographic evidence and modeling presented before provides strong indication that the 26°S lavas, particularly

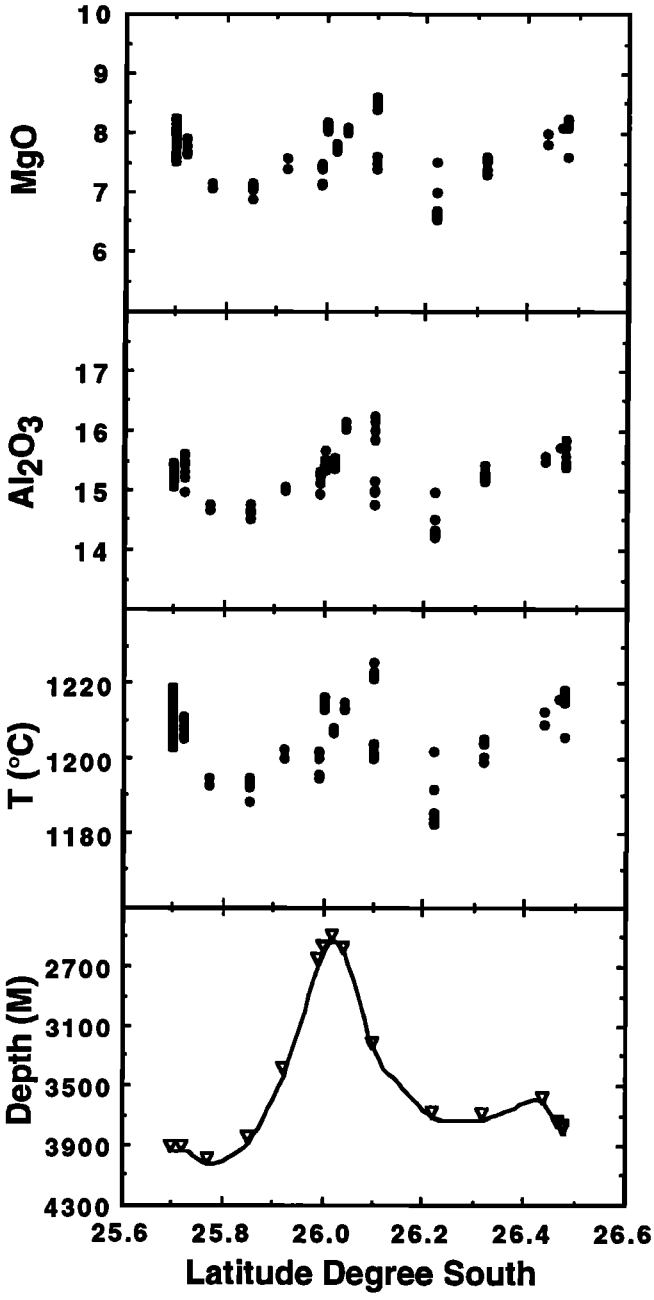

Figure 6. MgO, Al_2O_3, T(°C), and topography against latitude. The topography in the bottom panel uses dredge depth, and the triangles represent dredge locations projected onto the axis. Note the well-defined W-shaped along-axis patterns. Note also that except for the lavas near the offsets, there is a rough correlation between lava chemistry and axial depth, with high MgO lavas erupting at shallow depths. This is similar to what is normally found at the fast spreading East Pacific Rise [e.g., *Batiza and Niu*, 1992; *Scheirer and Macdonald*, 1993].

those of type I, have lost olivine, plagioclase and clinopyroxene at low pressure. However, several of the type I lavas also contain anorthitic megacrysts that may indicate fractionation at higher pressure as well. The lower CaO contents of Type II lavas are perhaps consistent with the loss of clinopyroxene expected to be important for polybaric fractionation at the pressure of the uppermost mantle [*Tormey et al.*, 1987; *Kinzler and Grove*, 1992; *Grove et al.*, 1992], but this would also result in lower TiO_2, not higher, as observed (Figure 5). Alternatively, high-pressure separation of plagioclase [*Bender et al.*, 1984; *Bryan et al.*, 1981; *Bryan*, 1983; *Tormey et al.*, 1987] is consistent with the higher TiO_2 but would deplete Al_2O_3 as well as CaO, which is not observed. While we cannot rule out the possibility of high pressure polybaric fractionation for either type I or type II lavas, we also do not find strong evidence for it in the petrography or chemistry of the lavas.

As the 26°S lavas are dominated by low-pressure phase assemblages, and given the important role of crustal magma chambers in the generation of ocean crust, even at slow spreading rates [e.g., *Sinton and Detrick*, 1992], it is reasonable to expect that the 26°S segment may possess such chambers. However, in view of the strong topographic and gravity evidence for higher magma supply in the middle of the 26°S segment [*Blackman and Forsyth*, 1991], it is likely that the style of magma storage varies along strike within the segment. Whether the existence of chambers is ultimately controlled by thermal structure [*Phipps Morgan and Chen*, 1993; *Hooft and Detrick*, 1993], melt buoyancy [*Ryan*, 1994], rheological properties of the country rocks, or some

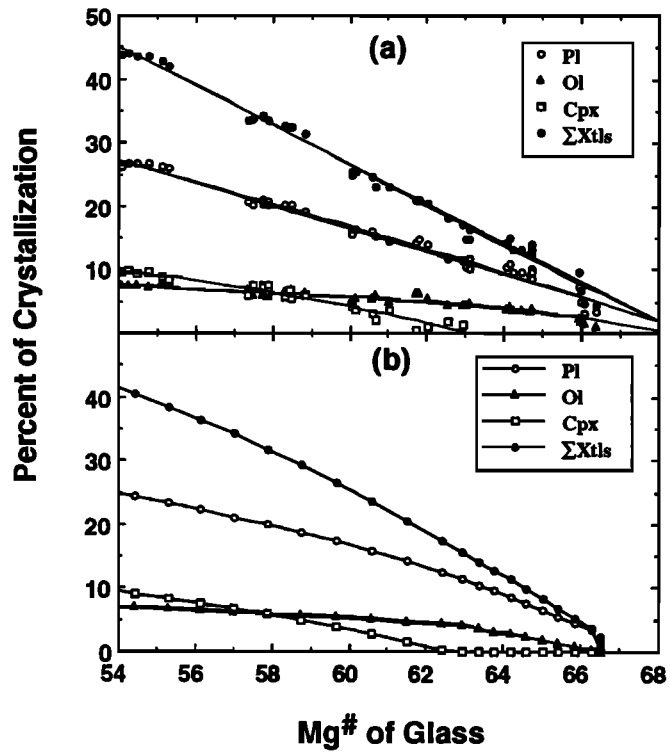

Figure 7. Fractionation model results, showing that type I lavas may be related by simple low pressure crystal fractionation. (a) Least squares mixing calculations as done by *Batiza and Niu* [1992] for all the type I samples (each point represents a sample) using the technique of *Bryan* [1986]. Mineral phase compositions used are from Tables 2, 3, and 4. (b) Liquid line of descent model calculations using the algorithm of *Weaver and Langmuir* [1990]. In both Figures 7a and 7b, the most primitive sample D21-4 was used as the "parent". Comparison between Figures 7a and 7b shows that the major element chemistry of type I lavas can be explained by low pressure fractional crystallization along a single liquid line of descent (LLD). Trace elements, however, are inconsistent with this idea, indicating that type I lavas (like type II) are derived from distinct, though similar, parental liquids.

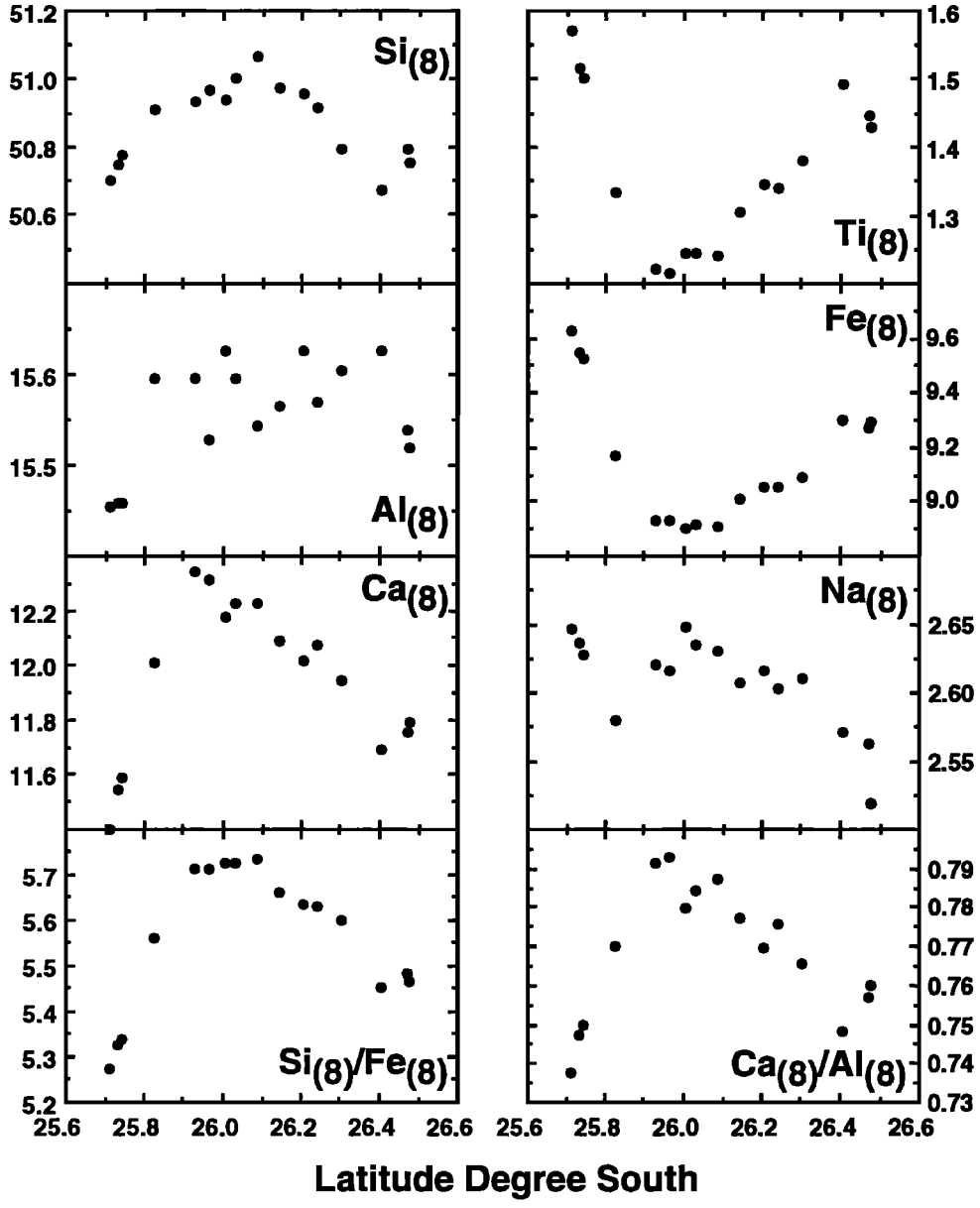

Figure 8. The oxides at MgO = 8.0 wt % plotted against latitude. The correction to MgO = 8.0 wt % was done using the algorithms of *Niu* [1992] (Table 7). The points plotted are the averages obtained with a moving boxcar filter [*Niu and Batiza*, 1991a] to enhance the first-order systematics. These plots show that most of the oxides display well defined trends, either concave downward ($Si_{[8]}$, $Ca_{[8]}$, $Si_{[8]}/Fe_{[8]}$, and $Ca_{[8]}/Al_{[8]}$), or concave upward ($Ti_{[8]}$ and $Fe_{[8]}$). $Al_{[8]}$ and $Na_{[8]}$ show no variations larger than analytical uncertainty. These patterns are interpreted qualitatively to indicate high extent of melting and low pressure of melting in the segment center and low extent of melting and high pressure of melting near offsets following *Niu and Batiza* [1991a, 1993].

Table 7. Fractionation Correction Coefficients

	SiO_2	TiO_2	Al_2O_3	FeO	CaO	Na_2O	K_2O	P_2O_5	Ni
m_1	-1.295	-1.9180	1.053	-8.0420	8.1173	0.5296	0.052	-0.175	80.72
m_2	0.061	0.1051	-0.010	0.4519	-0.5000	-0.0530	-0.004	0.010	-18.09
m_3									1.39

Oxides at MgO = 8.0 wt % were calculated following *Niu* [1992], which uses the general equation: $Ox_{[8]} = Ox_{[obs]} + \Sigma m_n(8^n - MgO^n)$, where $Ox_{[obs]}$ and $Ox_{[8]}$ are observed value of a non-MgO oxide and that of the corrected at MgO = 8.0 wt %, respectively. n is the order of regression, and m_n is the corresponding regression coefficients. The validity of the coefficients so determined is tested by showing (1) $\Sigma Ox_{[8]} + 8.0 = 100 \pm 1\%$; and (2) $Ox_{[8]}$ is independent of MgO.

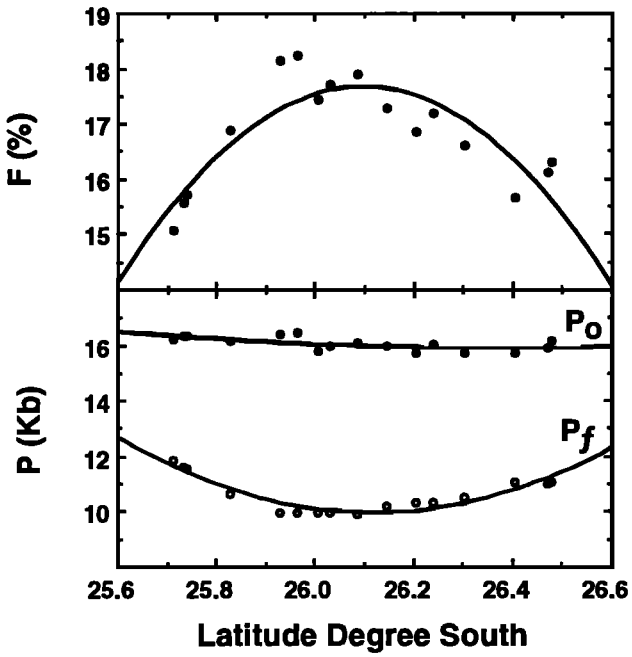

Figure 9. Calculated melting parameters against latitude, showing a maximum in the extent of melting on the north side of the segment center. The broad feature in F corresponds to a minimum in the final depth of melting (P_f). Note that the initial melting depth (P_o) is constant along axis, but the final depth of melting varies from ~12 kbar near offsets to ~10 kbar in the center of the segment. See text for discussion.

combination, it is to be expected that magma supply rate will exert a strong controlling influence. In this sense, along axis gradients in melt supply at 26°S may be analogous to those associated with propagating rift tips [e.g., *Sinton et al.*, 1983] or to the characteristic differences between slow and fast spreading centers [*Sinton and Detrick*, 1992].

Indeed, except for near the offsets, there is a reasonable correlation at 26°S between axial depth and MgO content, as observed along the East Pacific Rise [*Langmuir et al.*, 1986; *Batiza and Niu*, 1992; *Scheirer and Macdonald*, 1993]. The correlation is not perfect, as the highest MgO values occur not at the summit of the along-axis high, but on its southern slope. However, in general, high MgO lavas occur at shallow depths and vice-versa (Figure 6). In addition, the mean MgO content of lavas in the 26°S segment is lower than the high values characteristic of slow versus fast spreading ridges. These features at 26°S are unlike those observed farther south along the Mid-Atlantic Ridge by *Michael et al.*, [1994] and suggest that the shallow fractionation processes in the interior portions of the 26°S segment may be somewhat similar to those occurring below the East Pacific Rise. On the other hand, the evidence for multiple parental magma batches with distinct melting histories at 26°S is very different from the generally more homogenous parental melts found over equivalent lengths of the East Pacific Rise [*Langmuir et al.*, 1986; *Thompson et al.*, 1989; *Batiza and Niu*, 1992].

From the foregoing, it seems likely that magma chambers have played an important role in the interior portions of the 26°S segment. In the vicinity of the offsets, however, the evidence for such chambers is much weaker. The correlation between MgO and axial depth breaks down near both offsets, and the lavas tend to be generally more primitive. Thus if chambers exist in the vicinity of the offsets, they are probably smaller and have shorter magma residence times [*Sinton and Detrick*, 1992] than those in the interior of the segment, consistent with the inferred lower rates of magma supply near the offsets.

In summary, the 26°S lavas show mainly the petrographic and chemical effects of low-pressure fractionation, although higher-pressure polybaric fractionation cannot be precluded. In the interior of the segment, where there is evidence for higher magma supply rates, low-pressure fractionation may have occurred in chambers whose petrologic effects are not unlike those at the East Pacific Rise. However, near the offsets, with lower magma supply, chambers (if present) are probably much smaller and more typical of slow spreading

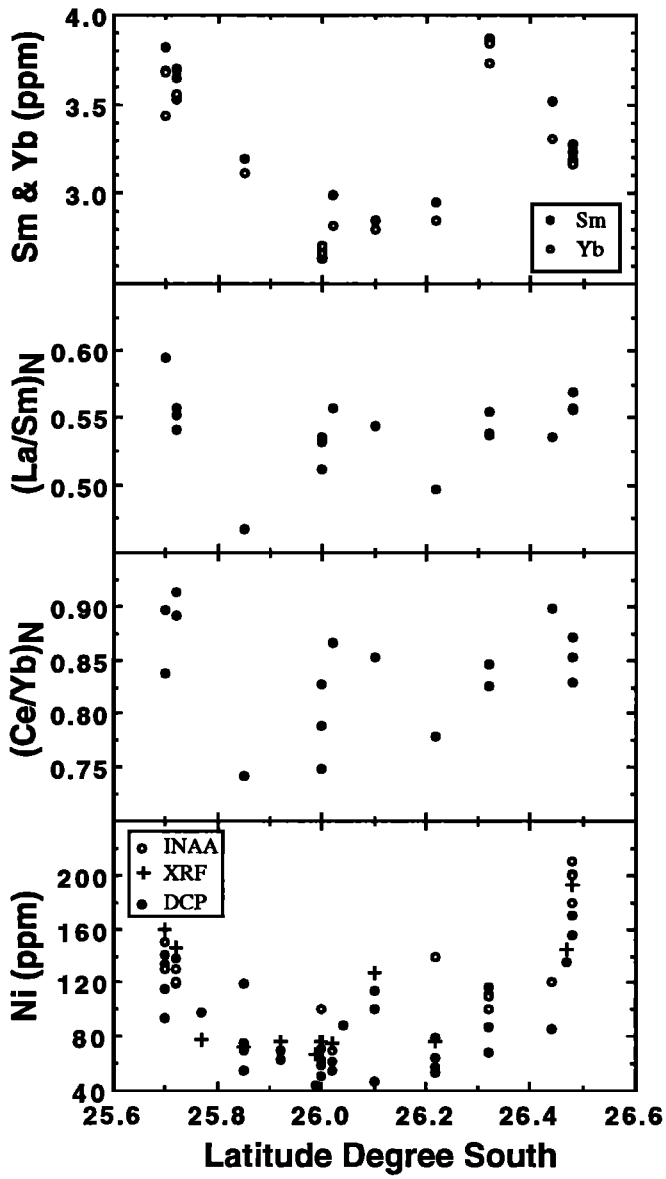

Figure 10. Representative trace element analyses plotted against latitude. The patterns for Ni, $[La/Sm]_N$, and $[Ce/Yb]_N$ show weaker and noisier W-shaped patterns than the major elements. In contract, rare earth element concentrations show U-shaped patterns like those of the normalized major elements (Figure 8) (additional XRF and DCP analyses for Ni are available from the authors or AGU as electronic supplement).

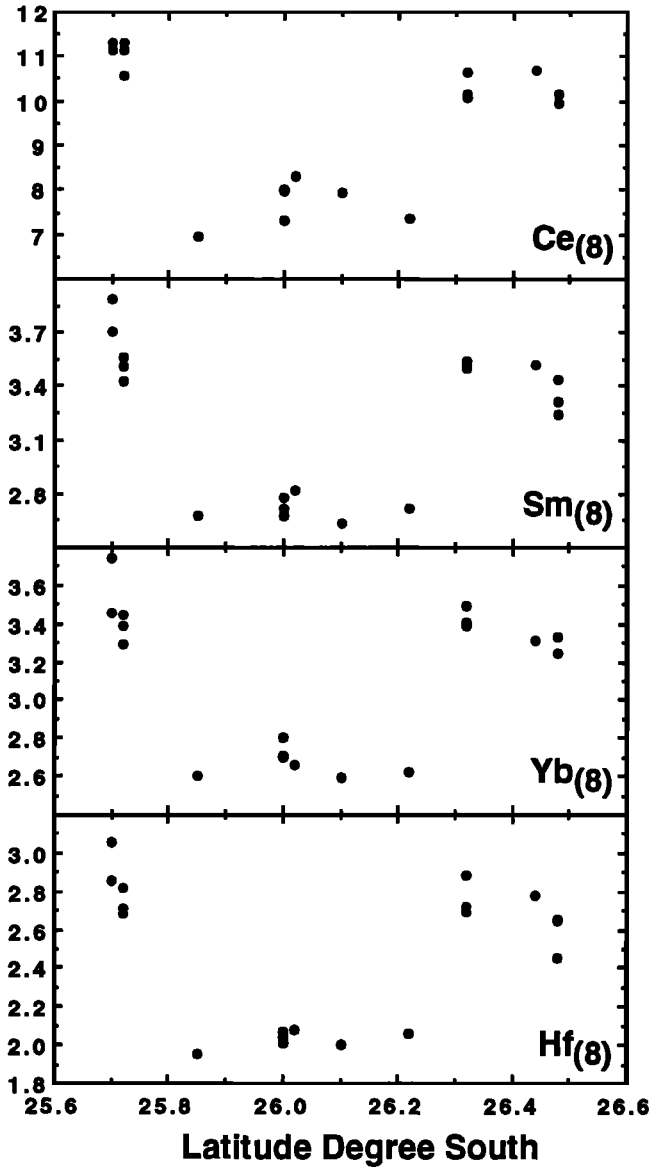

Figure 11. REE and Hf abundances at MgO = 8.0% against latitude, showing crude U-shaped patterns like those of Figure 8. These patterns consistently indicate that the lavas from the center represent higher extent of melting than those near offsets. The trace element concentrations at MgO = 8.0 % are calculated using the bulk K_d used in *Batiza and Niu* [1992].

ridges. In general, the segment appears to be supplied by multiple parental melt batches with distinct melting histories, which seemingly precludes extensive mixing in chambers and along-axis lateral transport. The magma supply architecture at 26°S thus seems to be significantly different from that proposed for the fast spreading East Pacific Rise [*Langmuir et al.*, 1986; *Macdonald et al.*, 1987, 1988; *Sinton et al.*, 1991; *Batiza and Niu*, 1992].

Mantle Heterogeneity

The 26°S segment is not affected by the influence of mantle plumes and lacks enriched basalts, unlike other ridge segments farther south along the Mid-Atlantic Ridge [*Michael et al.*, 1994]. Thus the mantle source of the 26°S melts lacks gross, first-order heterogeneity. Nevertheless, there is convincing evidence that it is not entirely homogeneous either. For example, the variations in isotopic values along the segment, while not large, are significant and show along-axis "W" and "M" patterns. The rough correlation among isotope ratios and trace element ratios (P. R. Castillo and D. W. Graham, in preparation, 1994) may indicate that isotopic and trace element heterogeneities are correlated. On the other hand, we cannot rule out the possibility that the abundances of the incompatible elements are due to complex melting phenomena, because of the observation that the abundances of some of the trace elements (e.g., the REE) and some of the key normalized major elements show U-shaped along-axis variation patterns (Figures 8 and 11). The unusual lack of correlation between $Ti_{[8]}$, $Na_{[8]}$, and $Al_{[8]}$ (Figure 8) in the 26°S lavas may be an indication of heterogeneity in the major element composition or modal mineralogy of the mantle source. This, however, is difficult to prove, as complex melting processes could conceivably produce similar results. Overall, there is good evidence that the mantle below the 26°S segment is heterogeneous, though the magnitude of chemical, modal, and isotopic variability is probably relatively small. Among other reasons, this heterogeneity is of interest because of its potentially important effects on melting and the possible complications to existing melting models [e.g., *Klein and Langmuir*, 1987; *Natland*, 1989; *Albarede*, 1992; Y. Shen and D. W. Forsyth, Geochemical constraints on initial and final depth of melting beneath mid-ocean ridges, submitted to *Journal of Geophysical Research*, 1994; hereinafter referred to as Y. Shen and D. W. Forsyth, submitted manuscript, 1994].

Extent of Melting, Melt Production and Crustal Thickness

Petrologic data can be used to estimate the extent of melting, in turn constraining models that relate mantle flow, melting and melt migration below ridges to the thickness of crust produced by these processes [e.g., *Forsyth*, 1992; *Turcotte and Phipps Morgan*, 1992; *Scott*, 1992; *Langmuir et al.*, 1992; *Forsyth*, 1993; Y. Shen and D. W. Forsyth, submitted manuscript, 1994]. Figure 9 shows the extent of melting (F) and the melting interval ΔP (P_o - P_f) we calculate for the 26°S lavas using the method of *Niu and Batiza* [1991a]. We calculate extents of melting that vary from ~15% near the offsets to ~18% in the middle of the segment, in qualitative agreement with estimates of thicker crust in the center of the segment [*Blackman and Forsyth*, 1991].

However, *Kinzler and Grove* [1993] show that *Niu and Batiza* [1991a] produce systematically higher F values than the models of *Langmuir et al.* [1987] and *Kinzler and Grove* [1992]. *Langmuir et al.* [1992] and *Forsyth* [1993] consider the F values of *Niu and Batiza* [1991a] to be the maximum extents of melting (F_{max}) experienced by any parcel of upwelling mantle. Their values for the mean extent of melting at 26°S would be 7.5–9% and 5–6%, respectively, much lower than our computed values of 15–18%. In order to determine which set of estimates is most likely to be correct, we consider a plot of $Ti_{[8]}/Na_{[8]}$ versus $Ti_{[8]}$ (Figure 12a). Since the ratio $Ti_{[8]}/Na_{[8]}$ decreases with decreasing $Ti_{[8]}$ (increasing extent of melting), it is clear that TiO_2 is behaving more incompatibly than Na_2O, contrary to widely accepted belief [see *Langmuir et al.*, 1992]. However bulk partition coefficients for TiO_2 and Na_2O from *Niu and Batiza* [1991*a*] and *Baker and Stolper* [1994] (Figure 12b) show that for this to be true, the mean extent of melting must be greater than ~15%. At F values below ~15%, Na_2O behaves

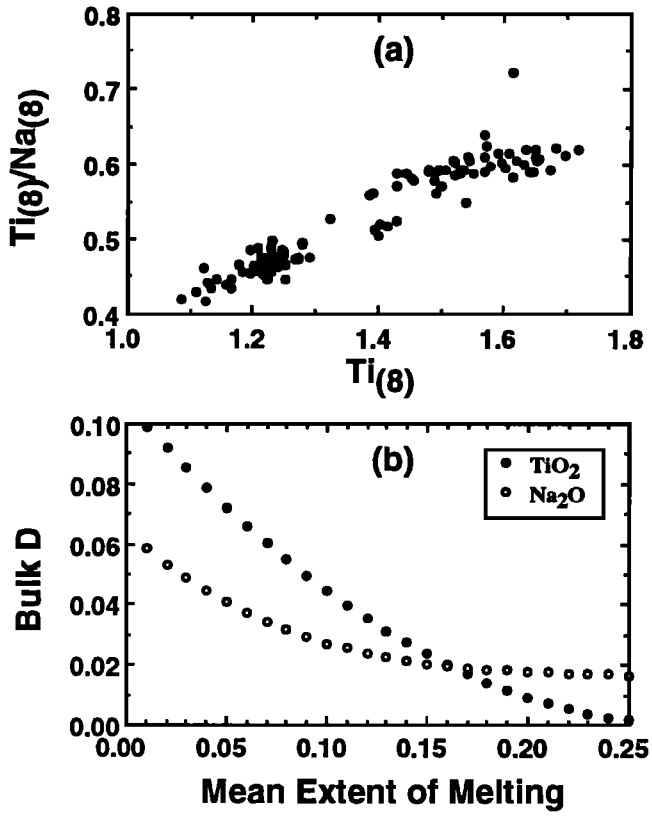

Figure 12. (a) $Ti_{[8]}/Na_{[8]}$ against $Ti_{[8]}$ for the 26°S lavas showing that Ti is more incompatible than Na, as Ti changes faster with melting (decreasing $Ti_{[8]}$) than Na. (b) Bulk *D* for both Na_2O and TiO_2 plotted as a function of mean extent of melting (or mean extent of depletion in mantle residue) during peridotite melting. The *D* values are from *Niu and Batiza* [1991a] and *Baker and Stolper* [1994]. It is obvious that both TiO_2 and Na_2O are incompatible during mantle melting, but Na_2O is more incompatible than TiO_2 at low extent of melting (F_{mean} < 15%). However, at extents of melting > 15%, the opposite is true. This suggests strongly that the lavas from 26°S, in which Ti is more incompatible than Na, represent mean extent of melting greater than 15%.

more incompatibly than TiO_2, the opposite of what we see at 26°S. This argues that our computed values of F are quite reasonable.

The models of *Forsyth* [1993] and *Langmuir et al.* [1992] give lower mean extents of melting because they explicitly consider shapes and flow regimes in the subaxial mantle region undergoing melting. This allows them to relate extent of melting to the crustal thickness. The model of *Niu and Batiza* [1991a] is much simpler and cannot be used to calculate crustal thickness because they consider only a simple column geometry and define F as the mass of melt / mass of mantle prior to melting. The fact that the estimates of F by this simple model appear to be more petrologically reasonable for 26°S may indicate that the scenarios considered by *Langmuir et al.* [1992] and *Forsyth* [1993] are inappropriate for the 26°S segment. One possibility is that the shape of the region undergoing melting is different from the triangular shape they consider. Another possibility is that the mantle does not simply flow upward passively, i.e., there is a component of buoyant upwelling as well [e.g., *Turcotte and Phipps Morgan,* 1992]. *Niu and Batiza* [1993] proposed 3-D, diapiric mantle upwelling to explain the chemical systematics of slow spreading ridges, like the 26°S segment. If this model is correct, as we argue below, it may partly explain why the *Niu and Batiza* [1991a] estimates of F appear to be correct.

Figure 9 also shows a rather narrow melting interval (P_o–P_f) of 5 to 6.5 kbar for the 26°S segment. This is because in contrast with other models, the model of *Niu and Batiza* [1991a] does not continue melting to the base of the crust or lithosphere. Instead, they estimate P_o and F independently and stop melting at P_f after the requisite amount of melt has been produced. As a consequence, the amount of melting that occurs as a result of adiabatic decompression (average of ~2–2.5%/kbar) is higher than other estimates [e.g., *Ahearn and Turcotte,* 1979; *Langmuir et al,* 1992] of a constant value of 1–1.2% / kb. These low values of melt production are required to match observed values of crustal thickness on the assumption of low melt retention in the mantle (i.e., all of the melt produced in the mantle contributes to crust production). However, the thermodynamic data needed to constraint these values are highly uncertain [e.g., *Yoder,* 1976] (also see *Hess* [1992] for discussion). Further, these values are almost certainly not constant, as progressive melting causes the mantle to become progressively more depleted and refractory. At some point the increasingly large heat of fusion will be higher than the energy provided by decompression and melting will stop. If conductive cooling is important [*Cordery and Phipps Morgan,* 1992; Y. Shen and D. W. Forsyth, submitted manuscript, 1994], and decompression is not perfectly adiabatic, then melting will also stop sooner.

Better estimates of the amount of melt produced by decompression melting will require much more complete information on the thermodynamic properties of minerals, rocks and melts under conditions of variable temperature, pressure and composition. However, we note that it is likely that melting stops well below the Moho, due to the combined effects of progressive depletion and conductive cooling. If so, then present estimates of melting of 1–1.2%/kbar are almost certainly too low. Given our present level of uncertainty, the values we estimate, while seemingly quite high, may actually be very reasonable.

The petrologic results of Figure 9 indicate lower extents of melting and a shorter melting column near offsets with higher extents of melting and taller melting columns below the center of the segment. The initial depth of melting is apparently constant (~16 kbar) and well within the spinel stability field, in agreement with observed REE abundances and ratios for reasonable melting scenarios (Figures 10 and 11). These results are thus consistent with gravity data [*Blackman and Forsyth,* 1991] and may be explained by weaker upwelling below offsets, together with a cold-edge effect [*Phipps Morgan and Forsyth,* 1988; Y. Shen and D. W. Forsyth, submitted manuscript, 1994]. The steeper gradient in F on the north side of the segment (Figure 9) is consistent with a cold edge because greater cooling would be expected across the Rio Grande transform (2.4 Ma offset) than across the Moore discontinuity (0.5 Ma offset).

Origin of the Local Trend

Batiza et al. [1988] and *Niu and Batiza* [1993] showed that the 26°S segment exhibits the chemical systematics called the local trend [*Klein and Langmuir,* 1989], as is characteristic for ridges spreading at rates < 50 mm/yr [*Niu and Batiza,* 1993]. Several explanations have been proposed for the trend [e.g.,

Langmuir et al., 1992; *Kinzler and Grove*, 1992], including that of *Niu and Batiza* [1993], who propose that it is due to melting in diapiric bodies of mantle via the reaction: melt A + pyroxene ⇒ melt B + olivine. This reaction [*Kelemen*, 1990] is a net melting reaction in which pyroxene enters the melt while olivine precipitates. *Niu and Batiza* [1993] propose that such a reaction may be enhanced by the smaller differential velocity between melt and solid residue accompanying buoyant diapiric upwelling and such 3-D upwelling below slow spreading ridges is supported by gravity and modeling studies [e.g., *Lin and Phipps Morgan*, 1992; *Parmentier and Phipps Morgan*, 1990].

Chemical data for the 26°S lavas provide additional evidence in favor of this idea. For example, Figure 13 shows that with progressive decompression (increasing $Si_{[8]}/Fe_{[8]}$) and melting, $Ti_{[8]}$ and $Ca_{[8]}$ behave in a complementary manner: CaO abundance increases as the abundance of TiO_2 decreases. The complementarity of this relationship strongly suggests control by clinopyroxene which is the most important source for both TiO_2 and CaO in the melt. Even more important is the evidence from Ni abundances (Figure 14) suggesting the contemporaneous precipitation of olivine.

Figure 14 shows that $Ni_{[8]}$ decreases with decompression (increasing $Si_{[8]}/Fe_{[8]}$) and continuous melting (increasing $Ca_{[8]}$ and decreasing $Ti_{[8]}$), suggesting that olivine, the primary host of Ni in the mantle, precipitates while pyroxene enters the melt. Assuming that fertile MORB mantle has Ni content 2200 ppm [e.g., *Hart and Zindler*, 1989], and a bulk distribution coefficient $D = 3$ during peridotite melting [e.g., *Lindstrom and Weill*, 1978], then the primary melts [see *Niu and Batiza*, 1991a, Table 6 and Figure 10] corresponding to the melting conditions of Figure 9 will have Ni contents of 760 ± 10 ppm. Taking a value of 10 for $K_d^{Ol}{}_{Ni}$ [*Hart and Davis*, 1978], the melts would have Ni contents of 300 ± 10 ppm after crystallizing olivine to MgO = 8.0 wt %. The deviation from 300 ppm of the mean $Ni_{[8]}$ values in Figure 14 would then be due to olivine precipitation during melting. Figure 15 shows the results and indicates that 9% to 15% olivine precipitation is required to explain the Ni data. These values are slightly lower than the value (~ 20%) calculated using major elements [*Niu and Batiza*, 1993]; however, considering the uncertainties involved in all these calculations, this agreement is actually quite good. The new data from 26°S thus provide strong additional support for the melting reaction and model of *Niu and Batiza* [1993].

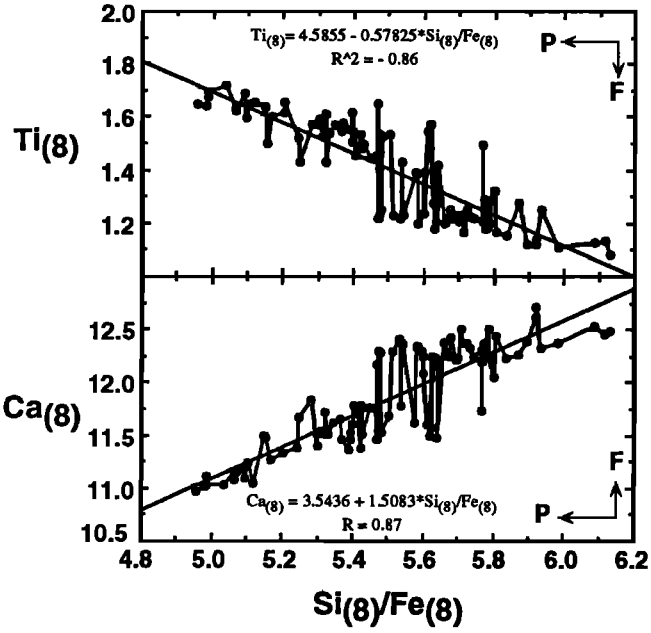

Figure 13. $Ti_{[8]}$ and $Ca_{[8]}$ versus $Si_{[8]}/Fe_{[8]}$ for the 26°S data. As clinopyroxene is the only mineral phase that buffers both Ti and Ca in the melting environment, the striking complementarity of the two curves indicates that clinopyroxene (also orthopyroxene) is being dissolved into the melt with decompression (increasing $Si_{[8]}/Fe_{[8]}$).

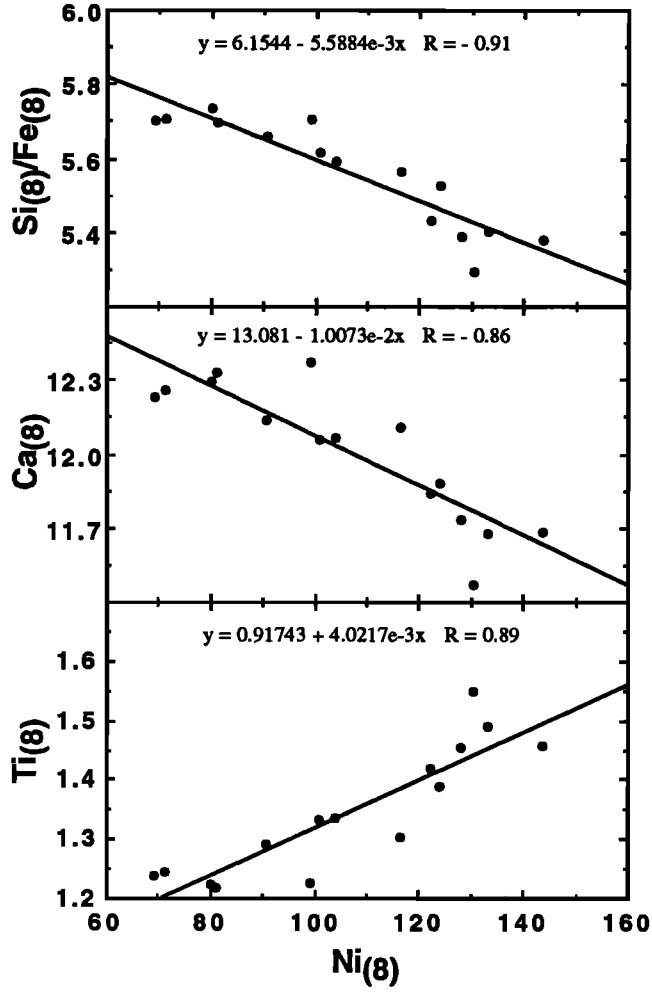

Figure 14. $Si_{[8]}/Fe_{[8]}$, $Ca_{[8]}$, and $Ti_{[8]}$ versus $Ni_{[8]}$ of averaged data with a moving boxcar filter (as for Figure 8). Each data point represents one dredge location (note that no trace element data available for dredge 26; very little sample). These correlations, statistically significant at ≥ 95% confidence level, suggest $Ni_{[8]}$ decreases with increasing melting (increasing $Ca_{[8]}$ and decreasing $Ti_{[8]}$) and decompression (increasing $Si_{[8]}/Fe_{[8]}$), which confirms that the reaction, melt A + pyroxene ⇒ melt B + olivine, is an important process in mantle melting dynamics at the slow spreading ridges [*Niu and Batiza*, 1993].

Petrogenetic Model for the 26°S Segment

The foregoing data and interpretations suggest that mantle upwelling and melting are more vigorous beneath the center of the 26°S segment and less vigorous below the offsets. Interestingly, there is a correlation between the melting

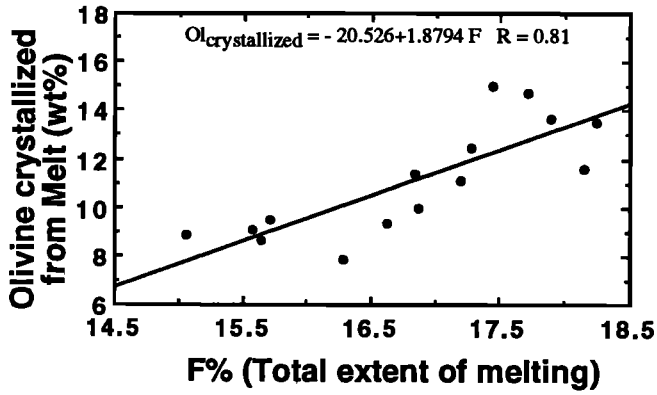

Figure 15. Olivine crystallization (wt %) from the melt versus total extent of melting (wt %), showing that the amount of the olivine crystallization during the overall melting is proportional to the extent of melting. See text for method used to calculate the Ni abundances and the amount of olivine crystallization.

parameters (F and P_f) of Figure 9 and values of the mantle Bouguer anomaly from *Grindlay et al.* [1992] (Figure 16), verifying the expected link between melting processes and crustal and upper mantle density structure [e.g., *Forsyth*, 1992].

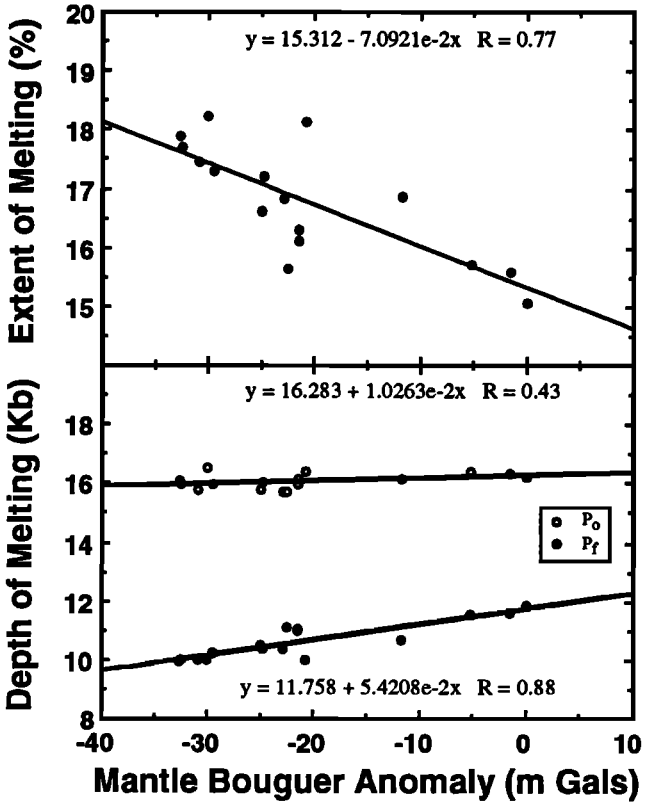

Figure 16. Extent of melting, and melting depths against mantle Bouguer anomaly (MBA) adapted from *Grindlay et al.* [1992]. It is clear that the observed mantle Bouguer anomaly (MBA) is related to melting process and melt production in the subaxial mantle. Although scattered, the inverse correlation between F(%) and MBA is significant. Note that MBA is essentially independent of initial depth of melting (P_0) but is correlated with final depth of melting, suggesting that the MBA is probably due to a shallow feature (≤ 50 km).

Figure 17 is a cartoon of the sort of model we favor for mantle flow, buoyant upwelling and melting, and melt tapping below the 26°S segment. We envision instabilities, perhaps of the Rayleigh-Taylor variety [*Ribe*, 1983; *Whitehead et al.*, 1984; *Schouten et al.*, 1985], developing at a common depth of ~50 km or deeper. These diapirs ascend because of buoyancy [e.g., *Oxburgh and Parmentier*, 1977; *Crane*, 1985; *Buck and Su*, 1989; *Scott and Stevenson*, 1989; *Niu and Batiza*, 1991b] and melt with decompression. The individual diapirs grow with ascent because of continuous melting and the possible entrainment of surrounding material [*Cawthorn*, 1975]. If these diapirs are tapped at different depths, then the erupted melts will have different chemical characteristics. For example, diapirs tapped at deep levels will have melts with low-F and high-P signatures, whereas diapirs tapped at shallow depth will have melts with high-F and low-P fingerprints, i.e., the local trend. The cold edge at 26°S may allow diking to deeper levels near the offsets, explaining the apparent deeper tapping of diapirs at the margins of the segment. Note that melting within individual diapirs is not perfect fractional melting but rather is between fractional and equilibrium melting as required by the solid-liquid reaction we propose. Significant melt retention is necessary for the solid-liquid reaction to occur during the ascent and melting of the diapirs.

Several aspects of the model are worth further discussion. First, this model invokes a constant depth of initial melting and is thus different from the models proposed by *Lin et al.* [1990], *Lin and Phipps Morgan* [1992] and previously by ourselves [*Niu and Batiza*, 1991a, 1993]. *Lin and Phipps Morgan* [1992] proposed a more 3-D focused upwelling (implying convex upward isotherms or concave upward mantle solidus) beneath slow-spreading ridge segments, however, the depressed solidus is not required by the petrological data from 26°S. This implies that mantle at depth may not necessarily be hotter in the center than near offsets, although the upwelling rate may be greater in the center than near offsets as suggested by *Phipps Morgan and Forsyth* [1988]. If P_0 is really constant along axis, then the mantle Bouguer anomaly would be a relatively shallow feature (≤ 50 km) at 26°S. The greater F and greater overall melt production in the center of the segment would result in greater density reduction of the mantle material and a greater volume of density-reduced mantle in the center of the segment than near offsets. Differential along-axis mantle upwelling and the cold edge effect both work in the same direction to produce the inferred density structure. We note that the 26°S segment may represent a special case and this model (Figure 17) may thus not apply to other slow spreading ridge segments in the Atlantic such as those at 27°–31°N [*Lin et al.*, 1990] and ~33°S [*Michael et al.*, 1994], where mantle upwelling may be focused and the solidus may be depressed in the segment center. This idea can be tested by further work at additional slow spreading segments.

We prefer multiple diapirs over focused upwelling and melting because the chemical data show that lavas from the 26°S segment display great petrogenetic diversity favoring many individual melt batches. In addition, diapirs of ~10 km in size are very common in mantle ophiolite terrains [*Nicolas*, 1989]. Finally, assuming that the crust is about twice as thick in the center as near the offsets at 26°S [*Blackman and Forsyth*, 1991], much greater melt production is required in the center of the segment than near the offsets is. This could be accomplished either with a greater upwelling rate or a wider upwelling zone in the segment center, or both.

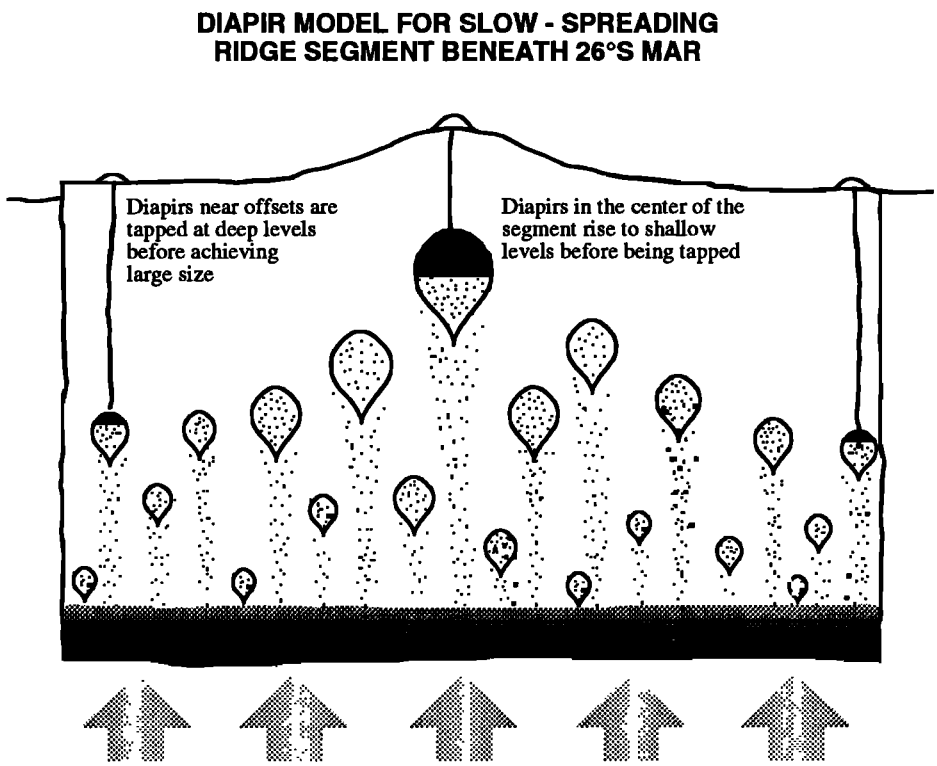

Figure 17. A cartoon showing an idealized along-axis cross section beneath the 26°S segment, with two bounding offsets and a central topographic high. In this model, the upwelling mantle begins to melt at a constant depth along the ridge axis. The solid areas in diapirs are melt which forms during ascent and the tiny dots show diapir trails. We invoke a lateral temperature gradient due to cold edges at the offsets, so dikes may penetrate to greater depths near offsets. Diapirs near offsets are tapped at deep levels before achieving large size and their melts are characterized by low extent of melting and high melting pressure. In contrast, diapirs in the center of the segment rise to shallow levels before being tapped, so their melts have the characteristics of large extents of melting and shallow melting pressure. See text for additional discussion.

Summary and Conclusions

The major conclusions of this study are as follows:

1. The segment at 26°S contains only depleted N-MORB lavas with typical petrographic characteristics and mineral chemistry. Type I lavas, mostly from the interior of the segment, crystallized plagioclase first, whereas type II basalts mostly from near the offsets, crystallized olivine first. Type I lavas achieve greater extents of fractionation, but both types are derived from petrogenetically diverse parental magmas.

2. The lavas are all dominated by low-pressure fractionation, though higher pressure, polybaric fractionation cannot be ruled out.

3. Except for lavas near the offsets, there is a rough correlation between lava chemistry and axial depth, similar to the relationship seen along the East Pacific Rise. Along-axis chemical variation for the segment as a whole shows "W" and "M" patterns, which we partly ascribe to greater melt supply in the center of the segment. Magma chambers in the center of the segment appear to be somewhat similar to those at fast spreading ridges, whereas those near offsets are more typical of slow spreading ones.

4. Some trace elements and isotope ratios also display W-shaped patterns of along-axis variation, but the REE and major elements normalized to 8 wt % show U-shaped patterns. The mantle source of the lavas is probably heterogeneous in major elements, trace elements, and isotopically; however, the extent of this variability is relatively small.

5. Melting calculations indicate that the extent of melting varies from ~15% near the offsets to ~18% in the middle of the segment. The depth of initial melting is roughly constant at ~50 km, but the depth of final melting is deeper under the offsets. Our inferred values of F are independently confirmed by variation of TiO_2 and Na_2O in the lavas and correlation between F and values of the mantle Bouguer anomaly.

6. Our interpretations are consistent with more vigorous upwelling and/or a wider zone of upwelling in the center of the segment. A cold edge effect at the offsets is also consistent with the petrologic results.

7. The 26°S segment, like other slow spreading ridges, exhibits the local trend of chemical variation. New data for Ni, CaO, TiO_2, and other elements strengthen the interpretation that the local trend is due to a melting reaction involving the melting of pyroxene and the coprecipitation of olivine.

8. The petrologic results at 26°S favor upwelling in buoyant diapirs, where melt and solid residue can interact. Melting and melt retention contribute to the buoyancy of the diapirs. Tapping of the diapirs is deeper near offsets than in the center of the segment, resulting in the chemical systematics of the local trend.

Acknowledgments. We greatly thank the captain, crew and scientific party of the R/V *Conrad* during RC2802, especially P. J. Fox and N. Grindlay. We thank W. Melson, T. O'Hearn, R. Korotev, and J. Karsten for their help in data collection, P. Castillo and D. Graham for providing unpublished isotope data. We also thank P. Castillo, S. Humphris, and J. Lin for valuable reviews. This study was supported by the Office of

Naval Research and the National Science Foundation. Y.N. gratefully acknowledges the support of an LDEO Postdoctoral Fellowship. This is SOEST contribution 3593 and LDEO contribution 5241.

References

Ahearn, J. L., and D. L. Turcotte, Magma migration beneath an ocean ridge, *Earth Planet. Sci. Lett.*, *45*, 115–122, 1979.

Albarède, F., How deep do common basaltic magmas form and differentiate?, *J. Geophys. Res.*, *97*, 10,997–11,009, 1992.

Baker, M. B., and E. M. Stoper, Determining the composition of high-pressure mantle melts using diamond aggregates, *Geochim. Cosmochim. Acta*, in press, 1994.

Batiza, R., and Y. Niu, Petrology and magma chamber processes at the East Pacific Rise ~ 9°30'N, *J. Geophys. Res.*, *97*, 6779–6797, 1992.

Batiza, R., W. G. Melson, and T. O'Hearn, Simple magma supply geometry inferred beneath a segment of the Mid-Atlantic Ridge, *Nature*, *335*, 428–431, 1988.

Batiza, R., P. J. Fox, P. R. Vogt, S. C. Cande, N. R. Grindlay, W. G. Melson, and T. O'Hearn, Morphology, abundance, and chemistry of near-ridge seamounts in the vicinity of the mid-Atlantic ridge ~ 26°S, *J. Geol.*, *97*, 209–220, 1989.

Batiza, R., Y. Niu, and P. Castillo, Magmatic segmentation in the South Atlantic — Petrological constraints at 26°S, *Eos Trans. AGU*, *71*, 624, 1990.

Bender, J. F., C. H. Langmuir, and G. N. Hanson, Petrogenesis of basalt glasses from the Tamayo region, East Pacific Rise, *J. Petrol.*, *25*, 213–254, 1984.

Blackman, D. K., and D. W. Forsyth, Isostatic compensation of tectonic features of the Mid-Atlantic Ridge: 25°–27°30'S, *J. Geophys. Res.*, *96*, 11,741–11,758, 1991.

Bryan, W. B., Systematics of model phenocrysts of submarine basalts, *Contrib. Mineral. Petrol.*, *83*, 62–74, 1983.

Bryan, W. B., Linked evolutionary data arrays: A logical structure for petrologic modelling of multisource, multiprocess magmatic systems, *J. Geophys. Res.*, *91*, 5891–5900, 1986.

Bryan, W. B., G. Thompson, and J. N. Ludden, Compositional variations in normal MORB from 22°–25°N: Mid-Atlantic Ridge and Kane Fracture Zone, *J. Geophys. Res.*, *86*, 11,815–11,836, 1981.

Buck, W. R., and W. Su, Focused mantle upwelling below mid-ocean ridges due to feedback between viscosity and melting, *Geophys. Res. Lett.*, *16*, 641–644, 1989.

Carbotte, S. M., S. M. Welch, and K. C. Macdonald, Spreading rate, rift valley propagation, and fracture zone offset history during the past 5 my on the Mid-Atlantic Ridge: 25°–27°30'S and 31° – 34°30'S, *Mar. Geophys. Res.*, *13*, 51–80, 1991.

Castillo, P. R., and R. Batiza, Mantle dynamics beneath the South Atlantic inferred from the Sr, Nd, and Pb isotope geochemistry of seamounts, *Nature*, *342*, 262–265, 1989.

Cawthorn, R. G., Degrees of melting in mantle diapirs and the origin of ultramafic liquids, *Earth Planet. Sci. Lett.*, *27*, 113–120, 1975.

Cordery, M. J., and J. Phipps Morgan, Melting and mantle flow beneath a mid-ocean ridge spreading center, *Earth Planet. Sci. Lett.*, *111*, 493–516, 1992.

Crane, K., The spacing of rift axis highs: Dependence on diapiric processes in the underlying asthenosphere?, *Earth Planet. Sci. Lett.*, *72*, 405–415, 1985.

Davis, A. S., and D. A. Clague, Geochemistry, mineralogy, and petrogenesis of basalt from the Gorda ridge, *J. Geophys. Res.*, *92*, 10,467–10,483, 1987.

Eaby, J. S., D. A. Clague, and J.-P. Eissen, Gabbroic xenoliths from the southern Juan de Fuca ridge: Implications for magma evolution at mid-ocean ridge spreading centers, *J. Geophys. Res.*, *91*, 3795–3820, 1986.

Elthon, D., Petrology of gabbroic rocks from the mid-Cayman rise spreading center, *J. Geophys. Res.*, *92*, 658–682, 1987.

Elthon, D., J. F. Casey, and S. Komor, Mantle chemistry of ultramafic cumulates from the North Arm Mountain Massif of the Bay of Islands ophiolite: Evidence for high-pressure crystal fractionation of oceanic basalts, *J. Geophys. Res.*, *87*, 8717–8734, 1982.

Fisk, M. R., A. E. Bence, and J.-G. Schilling, Major element chemistry of Galapagos rift zone magmas and their phenocrysts, *Earth Planet. Sci. Lett.*, *61*, 171–189, 1982.

Flower, M. J. F., Thermal and kinematic control on ocean-ridge magma fractionation: Contrasts between Atlantic and Pacific spreading axes, *J. Geol. Soc. London*, *138*, 695–712, 1980.

Forsyth, D. W., Geophysical constraints on mantle flow and melt generation beneath mid-ocean ridges, in *Mantle Flow and Melt Generation at Mid-Ocean Ridges*, *Geophys. Monogr. Ser.*, vol. 71, edited by J. Phipps Morgan, D. K. Blackman, and J. M. Sinton, pp. 1–66, AGU, Washington, D. C., 1992.

Forsyth, D. W., Crustal thickness and the average depth and degree of melting in fractional melting models of passive flow beneath mid-ocean ridges, *J. Geophys. Res.*, *98*, 16,073–16,079, 1993.

Fram, M. S., and J. Longhi, Phase equilibria of dikes associated with Proterozoic anorthosite complexes, *Am. Mineral.*, *77*, 605–616, 1992.

Gerlach, D. C., and T. L. Grove, Petrology of Medicine Lake Highland volcanics: Characterization of endmembers of magma mixing, *Contrib. Mineral. Petrol.*, *80*, 147–159, 1982.

Grindlay, N. R., P. J. Fox, and K. C. Macdonald, Second order ridge axis discontinuities in the South Atlantic: Morphology, structure, and evolution, *Mar. Geophys. Res.*, *13*, 21–49, 1991.

Grindlay, N. R., P. J. Fox, and P. R. Vogt, Morphology and tectonics of the Mid-Atlantic Ridge (25° – 27°30'S) from Sea Beam and magnetic data, *J. Geophys. Res.*, *97*, 6983–7010, 1992.

Grove, T. L., and W. B. Bryan, Fractionation of pyroxene-phyric MORB at low pressure: An experimental study, *Contrib. Mineral. Petrol.*, *84*, 293–309, 1983.

Grove, T. L., R. J. Kinzler, and W. B. Bryan, Fractionation of mid-ocean ridge basalt (MORB), in *Mantle Flow and Melt Generation at Mid-Ocean Ridges*, *Geophys. Monogr. Ser.*, vol. 71, edited by J. Phipps Morgan, D. K. Blackman, and J. M. Sinton, pp. 281–310, AGU, Washington, D. C., 1992.

Hanan, B. B., R. H. Kinsley, and J.-G. Schilling, Pb isotope evidence in the South Atlantic for migrating ridge hotspot interactions, *Nature*, *322*, 137–144, 1986.

Hart, S. R., and K. E. Davis, Nickel partitioning between olivine and silicate melt, *Earth Planet. Sci. Lett.*, *40*, 203–219, 1978.

Hart, S. R., and A. Zindler, Constraints on the nature and development of chemical heterogeneities in the mantle, in *Mantle Convection*, edited by W. R. Peltier, Gordon and Breach, New York, pp.261–387, 1989.

Hess, P. C., Phase equilibria constraints on the origin of ocean floor basalts, in *Mantle Flow and Melt Generation at Mid-Ocean Ridges*, *Geophys. Monogr. Ser.*, vol. 71, edited by J. Phipps Morgan, D. K. Blackman, and J. M. Sinton, pp. 67–102, AGU, Washington, D. C., 1992.

Hooft, E. E., and R. S. Detrick, The role of density in the accumulation of basaltic melt at mid-ocean ridges, *Geophys. Res. Lett.*, *20*, 423–426, 1993.

Humphris, S. E., G. Thompson, J.-G. Schilling, and R. H. Kingsley, Petrological and geochemical variations along the Mid-Atlantic Ridge between 46°S and 32°S: Influence of the Tristan de Cunha mantle plume, *Geochim. Cosmochim. Acta*, *49*, 1445-1464, 1985.

Kelemen, P. B., Reaction between ultramafic rock and fractionating basaltic magma, II, Experimental investigations of reaction between olivine tholeiite and harzburgite at 1150–1050°C and 5 kb, *J. Petrol.*, *31*, 99–134, 1990.

Kinzler, R. J., and T. L. Grove, Primary magmas of mid-ocean ridge basalts, 2, Applications, *J. Geophys. Res.*, *97*, 6907–6926, 1992.

Kinzler, R. J., and T. L. Grove, Corrections and further discussion of the primary magmas of mid-ocean ridge basalts, 1 and 2, *J. Geophys. Res.*, *98*, 22,339–22,347, 1993.

Klein, E. M., and C. H. Langmuir, Global correlations of ocean ridge basalt chemistry with axial depth and crustal thickness, *J. Geophys. Res.*, *92*, 8089–8115, 1987.

Klein, E. M., and C. H. Langmuir, Local versus global variation in ocean ridge basaltic composition: A reply, *J. Geophys. Res.*, *94*, 4241–4252, 1989.

Langmuir, C. H., J. F. Bender, and R. Batiza, Petrological and tectonic segmentation of the East Pacific Rise, 5°30'–14°30'N, *Nature*, *322*, 422–429, 1986.

Langmuir, C. H., E. M. Klein, and T. Plank, Petrological systematics of mid-ocean ridge basalts: Constraints on melt generation beneath ocean ridges, in *Mantle Flow and Melt Generation at Mid-Ocean Ridges*, *Geophys. Monogr. Ser.*, vol. 71, edited by J. Phipps Morgan, D. K. Blackman, and J. M. Sinton, pp. 183–280, AGU, Washington, D. C., 1992.

Lin, J., and J. Phipps Morgan, The spreading rate dependence of three-dimensional mid-ocean ridge gravity structure, *Geophys. Res. Lett.*, *19*, 13–16, 1992.

Lin, J., G. M. Purdy, H. Schouten, J.-C. Sempéré, and C. Zervas, Evidence from gravity data for focused magmatic accretion along the Mid-Atlantic Ridge, *Nature*, *344*, 627–632, 1990.

Lindstrom, D. J., and R. L. Korotev, TEABAGS: A computer program for instrumental neutron activation analysis, *J. Radioanal. Chem.*, *70*, 439–458, 1982.

Lindstrom, D. J., and D. F. Weill, Partitioning of transition metals between diopside and coexisting silicate liquids, 1, Nickel, cobalt, and manganese, *Geochim. Cosmochim. Acta, 42*, 817–831, 1978.

Macdonald, K. C., Mid-ocean ridges: Fine scale tectonic, volcanic, and hydrothermal processes within the plate boundary zone, *Annu. Rev. Earth Planet. Sci., 10*, 155–190, 1982.

Macdonald, K. C., J. C. Sempéré, P. J. Fox, and R. Tyce, Tectonic evolution of ridge axis discontinuities by the meeting, liking and self-decapitation of neighbouring ridge segments, *Geology, 15*, 993–997, 1987.

Macdonald, K. C., P. J. Fox, L. J. Perram, M. F. Eisen, R. M. Haymon, S. P. Miller, S. M. Carbotte, M.-H. Cormier and A. N. Shor, A new view of the mid-ocean ridge from the behaviour of ridge axis discontinuities, *Nature, 335*, 217–225, 1988.

Mahoney, J. J., J. M. Sinton, M. D. Kurz, J. D. Macdougall, K. J. Spencer, and G. W. Lugmair, Isotope and trace element characteristics of a super-fast spreading ridge: East Pacific Rise, 13 – 23 °S, *Earth Planet. Sci. Lett.*, in press, 1994.

Mevel, C., and D. Velde, Clinopyroxene in Mesozoic pillow lavas from the French Alps: Influence of cooling rate on compositional trends, *Earth Planet. Sci. Lett., 32*, 158–164, 1976.

Michael, P. J., et al., Mantle control of a dynamically evolving spreading center, *Earth Planet. Sci. Lett., 121*, 451–468, 1994.

Miller, D. M., J. F. Bender, and C. H. Langmuir, Gabbroic xenoliths from 9°20'N – 10°00'N on the East Pacific Rise suggest in situ crystallization, *Contrib. Mineral. Petrol.*, in press, 1994.

Morel, J. M., and R. Hékinian, Compositional variation of volcanics along segments of recent spreading ridges, *Contrib. Mineral. Petrol., 72*, 425–436, 1980.

Natland, J. H., Effects of axial magma chambers beneath spreading centres on the compositions of basaltic rocks, *Initial Rep. Deep Sea Drill. Proj., 54*, 833–850, 1980.

Natland, J. H., Partial melting of a lithologically heterogeneous mantle: Inferences from crystallization histories of magnesian abyssal tholeiites from the Siqueiros Fracture Zone, in Magmatism in Ocean Basins, edited by A. D. Saunders and M. J. Norry, *Geol. Soc. Spec. Publ., London, 42*, 41–70, 1989.

Nicolas, A., *Structures of Ophiolites and Dynamics of Oceanic Lithosphere*, 368 pp., Kluwer Academic, Norwell, Mass., 1989.

Nisbet, E. G., and J. A. Pearce, TiO_2 and a possible guide to past oceanic spreading rates, *Nature, 246*, 468–469, 1973.

Niu, Y., Mid-ocean ridge magmatism: Style of mantle upwelling, partial melting, crustal level processes, and spreading rate dependence — A petrologic approach, Ph.D. thesis, 250pp., Univ. of Hawaii, Honolulu, 1992.

Niu, Y., and R. Batiza, An empirical method for calculating melt compositions produced beneath mid-ocean ridges: Application for axis and off-axis (seamounts) melting, *J. Geophys. Res., 96*, 21,753–21,777, 1991a.

Niu, Y., and R. Batiza. In-situ densities of silicate melts and minerals as a function of temperature, pressure, and composition, *J. Geol., 99*, 767–775, 1991b.

Niu, Y., and R. Batiza, Chemical variation trends at fast and slow spreading ridges, *J. Geophys. Res., 98*, 7887–7902, 1993.

O'Hara, M. J., Primary magma and the origin of basalts, *Scott. J. Geol., 1*, 19–40, 1965.

Oxburgh, E. R., and E. M. Parmentier, Compositional and density stratification in the oceanic lithosphere-causes and consequences, *J. Geol. Soc. London, 133*, 343–354, 1977.

Parmentier, E. M., and J. Phipps Morgan, Spreading rate dependence of three-dimensional structure on oceanic spreading centers, *Nature, 348*, 325–328, 1990.

Phipps Morgan, J., and Y. J. Chen, The genesis of oceanic crust: Magma injection, hydrothermal circulation, and crustal flow, *J. Geophys. Res., 98*, 6283–6297, 1993.

Phipps Morgan, J., and D. W. Forsyth, Three-dimensional flow and temperature perturbations due to a transform offset: Effects on oceanic crustal upper mantle structure, *J. Geophys. Res., 93*, 2955–2966, 1988.

Rhodes, J. M., M. A. Dungan, D. P. Blanchard, and P. E. Long, Magma mixing at mid-ocean ridges: Evidence from basalts drilled near 22°N on the Mid-Atlantic Ridge, *Tectonophysics, 55*, 35–62, 1979.

Ribe, N. M., Diapirism in the Earth's mantle: Experiments on the motion of a hot sphere in a fluid with temperature-dependent viscosity, *J. Volcanol. Geotherm. Res., 16*, 221–245, 1983.

Roeder, P. L., and R. F. Emslie, Olivine-liquid equilibrium, *Contrib. Mineral. Petrol., 29*, 275–289, 1970.

Ryan, M. P., Neutral buoyancy and the structure of mid-ocean ridge magma reservoirs, *J. Geophys. Res., 98*, 22,321–22,338, 1993.

Salters, V. J. M., and S. R. Hart, The hafnium paradox and the role of garnet in the source of mid-ocean ridge basalts, *Nature, 342*, 420–422, 1989.

Scheirer, D. S., and K. C. Macdonald, Variation in cross-section area of the axial ridge along the East Pacific Rise: Evidence for the magmatic budget of a fast spreading center, *J. Geophys. Res., 98*, 7871–7885, 1993.

Schilling, J.-G., G. Thompson, R. H. Kingsley, and S. E. Humphris, Hotspot-migrating ridge interactions along the South Atlantic: Geochemical evidence, *Nature, 313*, 187–191, 1985.

Schouten, H, K. D. Klitgord, and J. A. Whitehead, Segmentation of mid-ocean ridges, *Nature, 317*, 225–229, 1985.

Scott, D. R., Small-scale convection and mantle melting beneath mid-ocean ridges, in *Mantle Flow and Melt Generation at Mid-Ocean Ridges, Geophys. Monogr. Ser.*, vol. 71, edited by J. Phipps Morgan, D. K. Blackman, and J. M. Sinton, pp. 327–352, AGU, Washington, D. C., 1992.

Scott, D. R., and D. J. Stevenson, A self-consistent model of melting, magma migration and buoyancy-driven circulation beneath mid-ocean ridges, *J. Geophys. Res., 94*, 2973–2988,1989.

Sempéré, J.-C., G. M. Purdy, and H. Schouten, Segmentation of the Mid-Atlantic Ridge between 24°40'N and 30°40'N, *Nature, 344*, 427– 431, 1990.

Sinton, J. M., and R. S. Detrick, Mid-ocean ridge magma chambers, *J. Geophys. Res., 97*, 197–216, 1992.

Sinton, J. M., D. S. Wilson, D. M. Christie, R. N. Hey, and J. R. Delaney, Petrologic consequences of rift propagation on oceanic spreading ridges, *Earth Planet. Sci. Lett., 62*, 193–207, 1983.

Sinton, J. M., S. M. Smaglik, J. J. Mahoney, and K. C. Macdonald, Magmatic processes at superfast spreading ridges: Glass compositional variations along the East Pacific Rise 13°–23°S, *J. Geophys. Res., 96*, 6133–6155, 1991.

Smith, D. K., and J. R. Cann, Hundreds of small volcanoes on the medium valley floor of the Mid-Atlantic Ridge at 24° – 30°N, *Nature, 348*, 427–431, 1990.

Stakes, D. S., J. W. Shervais, and C. A. Hopson, The volcanic-tectonic cycle of the FAMOUS and AMAR valleys, Mid-Atlantic Ridge (36°47'N): Evidence from basalt glass and phenocryst compositional variations for a steady state magma chamber beneath valley midsections, AMAR 3, *J. Geophys. Res., 89*, 6995–7028, 1984.

Sun, S.-S., and W. F. McDonough, Chemical and isotopic systematics of ocean basalt: Implications for mantle composition and processes, in Magmatism of the Ocean Basins, edited by A. D. Saunders, and M. J. Norry, *Geol. Soc. Spec. Publ., London , 42*, 323–345, 1989.

Thompson, G., W. B. Bryan, and S. E. Humphris, Axial volcanism on the East Pacific Rise, 10°–12°N, in Magmatism in the Ocean Basin, edited by A. D. Saunders and M. J. Norry, *Geol. Soc. Spec. Publ., London, 42*, 181–200, 1989.

Tormey, D. R., T. L. Grove, and W. B. Bryan, Experimental petrology of normal MORB near the Kane Fracture Zone: 22°–25°N, Mid-Atlantic Ridge, *Contrib. Mineral. Petrol., 96*, 121–139, 1987.

Turcotte, D. L., and J. Phipps Morgan, The physics of magma migration and mantle flow beneath a mid-ocean ridge in *Mantle Flow and Melt Generation at Mid-Ocean Ridges, Geophys. Monogr. Ser.*, vol. 71, edited by J. Phipps Morgan, D. K. Blackman, and J. M. Sinton, pp. 155–182, AGU, Washington, D. C., 1992.

Walker, D., T. Shibata, and S. E. DeLong, Abyssal tholeiites from the Oceanographer Fracture Zone, II, Phase equilibria and mixing, *Contrib. Mineral. Petrol., 70*, 111–125, 1979.

Weaver, J. S., and C. H. Langmuir, Calculation of phase equilibrium in mineral-melt systems, *Comput. Geosci., 16*, 1–19, 1990.

Whitehead, J. A., H. J. B. Dick, and H. Schouten, A mechanism for magmatic accretion under spreading centres, *Nature, 312*, 146–147, 1984.

Yoder, H. S., Jr., *Generation of Basaltic Magma*, 265 pp., National Academy Press, Washington, D. C., 1976.

R. Batiza, Department of Geology and Geophysics, University of Hawaii, Honolulu, HI 96822. (e-mail: rbatiza@soest.hawaii.edu)

Y. Niu, Department of Earth Sciences, University of Queensland, Brisbane, Qld 4072, Australia. (e-mail: niu@earthsciences.uq.edu.au)

(Received December 9, 1993; revised June 13, 1994;
accepted June 22, 1994.)